Geophysical Journal International

Geophys. J. Int. (2017) **209,** 1800–1830
Advance Access publication 2017 March 23
GJI Geodynamics and tectonics

doi: 10.1093/gji/ggx126

Megathrust and accretionary wedge properties and behaviour in the Makran subduction zone

Camilla Penney,[1] Farokh Tavakoli,[2] Abdolreza Saadat,[2] Hamid Reza Nankali,[2] Morteza Sedighi,[2] Fateme Khorrami,[2] Farhad Sobouti,[3] Zahid Rafi,[4] Alex Copley,[1] James Jackson[1] and Keith Priestley[5]

[1]*COMET, Bullard Labs Department of Earth Sciences, University of Cambridge, Cambridge, United Kingdom. E-mail: cp451@cam.ac.uk*
[2]*Geodynamic Department, National Cartographic Center, P.O. Box* 13185-1684*, Meraj Ave., Tehran, Iran*
[3]*Department of Earth Sciences, Institute for Advanced Studies in Basic Sciences (IASBS), P.O. Box* 45195-1159*, Zanjan, Iran*
[4]*National Seismic Monitoring Centre, Pakistan Meteorological Department, P.O. Box* 1214*, Sector H-* 8/2*, Islamabad* 44000*, Pakistan*
[5]*Bullard Labs Department of Earth Sciences, University of Cambridge, Cambridge, United Kingdom*

Accepted 2017 March 22. Received 2017 March 21; in original form 2016 September 16

SUMMARY

We study the Makran subduction zone, along the southern coasts of Iran and Pakistan, to gain insights into the kinematics and dynamics of accretionary prism deformation. By combining techniques from seismology, geodesy and geomorphology, we are able to put constraints on the shape of the subduction interface and the style of strain across the prism. We also address the long-standing tectonic problem of how the right-lateral shear taken up by strike-slip faulting in the Sistan Suture Zone in eastern Iran is accommodated at the zone's southern end. We find that the subduction interface in the western Makran may be locked, accumulating elastic strain, and move in megathrust earthquakes. Such earthquakes, and associated tsunamis, present a significant hazard to populations around the Arabian Sea. The time-dependent strain within the accretionary prism, resulting from the megathrust earthquake cycle, may play an important role in the deformation of the Makran region. By considering the kinematics of the 2013 Balochistan and Minab earthquakes, we infer that the local gravitational and far-field compressive forces in the Makran accretionary prism are in balance. This force balance allows us to calculate the mean shear stress and effective coefficient of friction on the Makran megathrust, which we find to be 5–35 MPa and 0.01–0.03, respectively. These values are similar to those found in other subduction zones, showing that the abnormally high sediment thickness in the offshore Makran does not significantly reduce the shear stress on the megathrust.

Key words: Seismic cycle; Seismicity and tectonics; Rheology and friction of fault zones; Subduction zone processes; Asia.

1 INTRODUCTION

The Makran, formed by the subduction of the Arabian plate beneath the southern coasts of Iran and Pakistan, is one of the world's least well documented subduction zones. Logistical constraints have made much of the Makran essentially inaccessible in recent years, curtailing earlier field investigations (e.g. Harrison 1943; Falcon 1974; Harms *et al.* 1982). Only a small number of recent field studies have been conducted, looking at the morphology and geology of the region (e.g. Ellouz-Zimmermann *et al.* 2007; Haghipour *et al.* 2012). There is little onshore seismic data, and GPS measurements are sparse. As such, many aspects of the Makran's tectonics remain enigmatic. By combining techniques and results from seismology, geomorphology, GPS and modelling, we are able to gain insights into some of the fundamental questions about this subduction zone.

The seismic hazard posed by the Makran megathrust is one such question (e.g. Musson 2009; Smith *et al.* 2013). Subduction megathrusts host many of the world's largest earthquakes, and the hazard associated with such an event on this megathrust is potentially severe. If the earthquake were to cause a tsunami it could threaten densely populated coastal regions in Pakistan and western India (Bilham *et al.* 2007) and the Omani coast, which is undergoing rapid urbanization (Heidarzadeh & Kijko 2011). A significant part of the subduction interface in the eastern (Pakistani) Makran is locked and can produce large earthquakes. This locking was demonstrated by an M_w 8.1 earthquake on 1945 November 27, near Pasni (Ambraseys & Melville 1982; Fig. 1), which caused a small tsunami (Hoffmann *et al.* 2013). In contrast, the western (Iranian) Makran shows an almost total absence of shallow thrust earthquakes in both the instrumental and historical periods, with reports of only a single possible megathrust earthquake in 1483 (Ambraseys & Melville 1982),

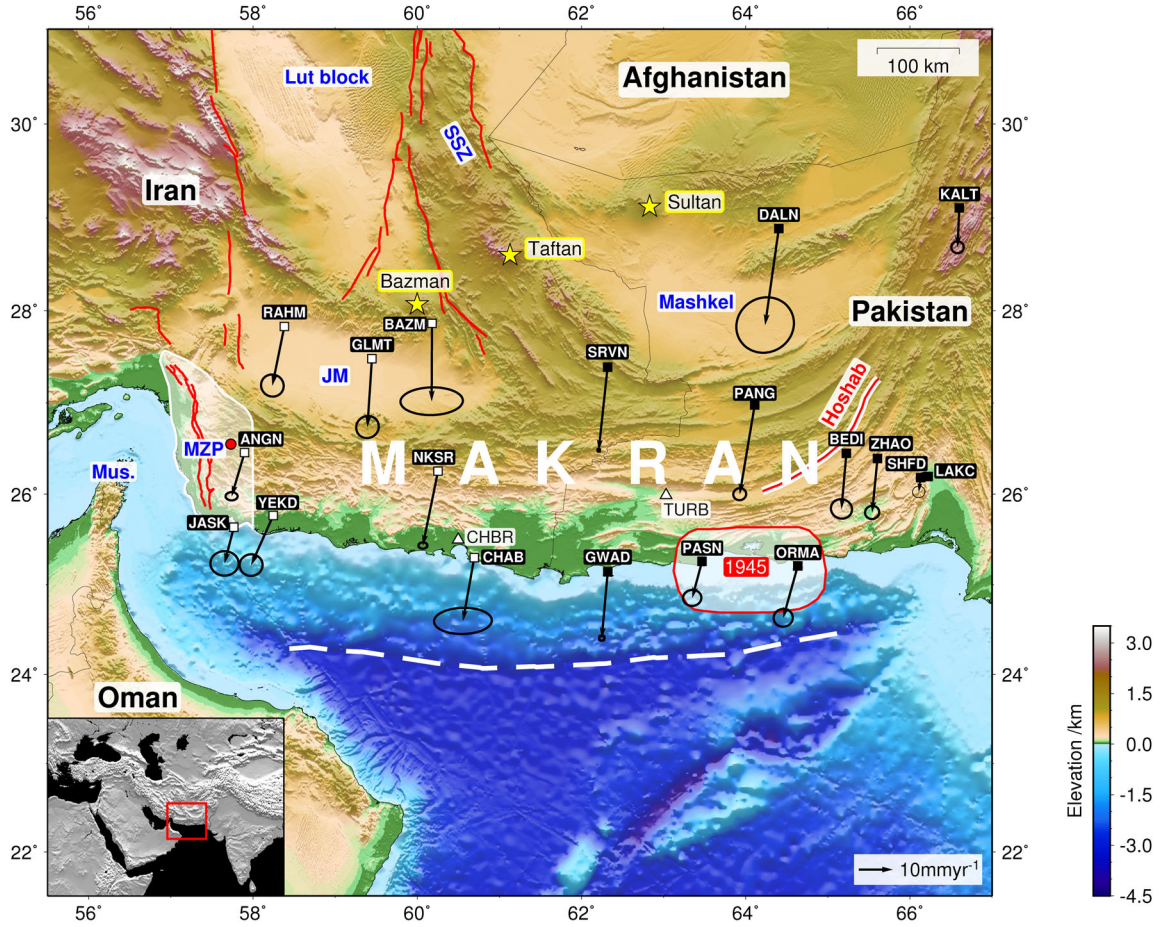

Figure 1. Map of the Makran region, location shown in the inset. Red lines are mapped strike-slip faults in SE Iran (Walker & Jackson 2004; Regard *et al.* 2005). SSZ is the Sistan Suture Zone and MZP is the Minab-Zendan-Palami fault zone. The white region surrounding the MZP shows the extent of mapped diffuse strike-slip faulting, which includes E–W oriented faults to the east of the MZP (Penney *et al.* 2015). The location of the 2013 Minab earthquake is shown by a red circle. The red line outlined in white is the trace of the surface ruptures of the 2013 Balochistan (Pakistan) earthquake on the Hoshab fault (Avouac *et al.* 2014). The red outlined region shows the approximate rupture area of the 1945 M_w 8.1 earthquake from Byrne *et al.* (1992). The white dashed line indicates the bathymetric break in slope at the toe of the accretionary wedge. Yellow stars show the volcanic centres associated with subduction. White triangles show the locations of seismometers, CHBR and TURB, which are used here for receiver-function analysis. The Jaz Murian (JM) and Mashkel depressions are labelled. Mus. is the Musandam Peninsula. Black arrows are GPS velocity vectors relative to Arabia with 95 per cent confidence ellipses. GPS velocities are taken from Vernant *et al.* (2004); Bayer *et al.* (2006); Masson *et al.* (2007); Peyret *et al.* (2009); Walpersdorf *et al.* (2014); Frohling & Szeliga (2016) and this paper. For stations with multiple reported velocities (BAZM, CHAB, JASK) we use a mean velocity; since the velocities reported by different authors are very similar, mostly within error of each other, this does not affect our results. Those GPS stations shown with white squares are used to model locking of the subduction interface in the western Makran (Section 3).

for which the source region is poorly constrained (Musson 2009). However, Ambraseys & Melville (1982) also note that the sparse population of the Makran throughout the historical period means that earthquakes in the region may not have been documented. A microseismic study using ocean bottom seismometers found no microseismicity in the western Makran (Niazi *et al.* 1980). This has led to suggestions that the megathrust in the western Makran may be sliding continuously, rather than accumulating elastic strain (Byrne *et al.* 1992). However, the distribution of large boulders along the Omani coast, thought to have been emplaced by tsunamis (Hoffmann *et al.* 2015), suggests that the megathrust in the western Makran may move in infrequent large earthquakes. A series of terraces along the Makran coast (Page *et al.* 1979) could have resulted from uplift in earthquakes, but could also be due to aseismic underplating and uplift (Platt *et al.* 1985). Whether the western Makran is locked and able to generate large earthquakes therefore remains an open question.

The mean dip of the subduction interface in the Makran is another open question. Geodetic data have been used to assess the degree of elastic strain accumulation in many other subduction zones, but this procedure requires a model for the shape and location of the subduction interface. Early results from seismic reflection surveys gave the dip of the oceanic plate Moho as less than 2° at ∼62.5°E (White & Louden 1982). Subsequent studies have revised this estimate to ∼3° in the same area, based on controlled-source seismic imaging of the sediment-basement interface (Kopp *et al.* 2000; Smith *et al.* 2012), which is thought to approximately coincide with the subduction interface (e.g. Kopp *et al.* 2000). A shallow dipping subduction interface in the western Makran has been proposed as an explanation for the small number of earthquakes in the region (Dykstra & Birnie 1979; Niazi *et al.* 1980). However, the curvature of subducting slabs makes the dip of the subduction interface near the toe of the wedge unrepresentative of the mean dip, and Maggi *et al.* (2000) proposed a 'true dip' of 26° at latitudes north of 27°N,

based on earthquake depths. Byrne *et al.* (1992) suggested that the dip of the subducting slab in the western Makran is likely to be steeper than in the east due to the smaller prism width and more southerly location of the volcanic arc in the west (Fig. 1). Frohling & Szeliga (2016) recently modelled GPS velocities in the region and concluded that the Makran megathrust is locked to a depth of at least 38 km. However, there are significant uncertainties in their proposed interface geometry, making it important to revisit this issue. We first present a compilation of earthquakes in the region, which we use to improve the constraints on the shape and location of the subduction interface (Section 2). This allows us to address the question of whether elastic strain accumulation in the western Makran is consistent with the available GPS data (Section 3).

Whether or not the plate interface in the western Makran is accumulating elastic strain has implications for another unresolved question in the region; how right-lateral shear across the Sistan Suture Zone (SSZ) is accommodated at the southern end of the mapped strike-slip faults. The SSZ, to the north of the Makran (Fig. 1), is an abandoned accretionary prism formed by the closure of a branch of the Neo-Tethys at 65–90 Ma (Tirrul *et al.* 1983; Bröcker *et al.* 2013). The rocks of the SSZ are now offset right-laterally by a series of NNW–SSE striking strike-slip faults, referred to collectively by Walpersdorf *et al.* (2014) as the East Lut fault, which have been active in the Plio-Quaternary (Tirrul *et al.* 1983; Walker & Jackson 2004). These faults accommodate 5–15 mm yr^{-1} of differential motion between the Lut Block (in the eastern part of Central Iran) and Afghanistan (Fig. 1), which moves as part of Eurasia (Vernant *et al.* 2004; Walker & Jackson 2004; Reilinger *et al.* 2006; Meyer and Le Dortz 2007; Walpersdorf *et al.* 2014). The ∼N–S striking faults are not observed south of ∼27°N, and no major N–S faults cut the E–W trending structures of the Makran ranges (Fig. 1; Jackson & McKenzie 1984; Walker *et al.* 2013), leading to the long-standing tectonic question of how right-lateral motion is accommodated at the SSZ's southern end. We present three possible solutions, discuss their kinematic implications and suggest which is most consistent with the available information (Section 4).

The Makran hosts the world's largest sub-aerial accretionary prism (Fruehn *et al.* 1997; Fig. 1). The sediments in this prism are thought to derive from the Proto-Indus fan (Harms *et al.* 1982) and have been thickened as the Arabian plate has subducted northwards. The extensive (∼200 × 1000 km) onshore part of the prism provides an ideal setting in which to study prism deformation. The offshore part of the accretionary prism, near the Musandam peninsula and the Omani coast, was imaged using seismic reflection and refraction experiments in the 1970s and early 1980s (e.g. White & Klitgord 1976; White & Louden 1982) and the eastern offshore section has been the subject of recent research (e.g. Kukowski *et al.* 2000; Smith *et al.* 2012). Offshore seismic data, and onshore geological studies give a time-integrated picture of the deformation but do not constrain the evolution of the prism through time. Prism evolution is controlled by both the forces acting on the prism, which may be time-dependent, and the prism's response to these forces, which is controlled by the behaviour of faults and folds within the prism and the rheology of the underlying megathrust. In addition to placing constraints on the shape and location of the subduction interface, our earthquake compilation allows us to assess the style of strain across the accretionary prism. By considering the present day style of strain, and the kinematics of the 2013 Balochistan and Minab earthquakes we infer that the prism has reached the maximum elevation which can be supported by the megathrust. We then use this information to estimate the average shear stress and effective coefficient of friction on the megathrust (Section 5).

2 SHAPE AND LOCATION OF THE SUBDUCTION INTERFACE

The mean dip of the subduction interface is important for assessing the degree of elastic strain accumulation on the interface (Section 3). To address this question, we present a compilation of well-located earthquakes in the Makran (Section 2.1), and receiver functions from local seismometers (Section 2.2), in order to constrain the range of possible dips of this interface (Section 2.3). Our compilation of earthquakes also allows us to infer the style of strain across the prism (Section 5).

2.1 Earthquake compilation

We use teleseismic body-waveform modelling and previously published results (from teleseismic body-waveform modelling, *P*-wave first motions and global earthquake catalogues) to produce a compilation of earthquakes with well-constrained depths and mechanisms. The criteria for a 'well-constrained' earthquake from each data set are discussed below. A table giving the depths, locations and mechanisms (where available) of well-constrained earthquakes is given in Appendix A. Fig. 2(a) shows earthquakes, $m_b > 4$, from 1945–2013 with published focal mechanisms (including earthquakes for which we consider the depth and/or focal mechanism to be poorly constrained, shown as semi-transparent). Fig. 2(b) shows earthquakes, $m_b > 4$, over the same time period, with well-constrained depths, and, where available, focal mechanisms.

Earthquake depths and mechanisms from teleseismic body-waveform modelling (McCaffrey & Abers 1988; McCaffrey *et al.* 1991) are well-constrained, with typical errors of ±10° in strike, ±5° in dip, ±10° in rake and ±4 km in depth (Molnar & Lyon-Caen 1989). Where available, we use published earthquake depths and mechanisms from this technique (Laane & Chen 1989; Byrne *et al.* 1992; Baker 1993; Berberian *et al.* 2000; Maggi *et al.* 2000; Berberian *et al.* 2001; Walker 2003; Engdahl *et al.* 2006; Jackson *et al.* 2006; Talebian *et al.* 2006; Nissen *et al.* 2010, 2011; Walker *et al.* 2013; Barnhart *et al.* 2014b; Jolivet *et al.* 2014; Penney *et al.* 2015). In addition, we have used teleseismic *P* and *SH* body-waveform modelling to determine the depths and focal mechanisms of seven earthquakes for which solutions have not previously been published (Figs B1–B7). The details of this technique have been discussed extensively elsewhere (e.g. Taymaz 1990; Maggi *et al.* 2000; Craig *et al.* 2014), and will not be reproduced here. Our solutions from this technique, and a more detailed discussion of the methodology, are presented in Appendix B. In particular, we have included our body-waveform modelling determined depth and focal mechanism for the M_w 6.3 2017 February 7 earthquake (Fig. B1), which occurred near the western Pakistani coast. This earthquake is also included in Figs 2(a) and (b), in the cluster of shallow thrusts near the Pakistani coastline.

For earthquakes which pre-date the widespread use of body-waveform modelling we use focal mechanisms determined from *P*-wave first motions by Jackson & McKenzie (1984); Jacob & Quittmeyer (1979) and Byrne *et al.* (1992). We consider first-motion solutions to be well-constrained if depth phases are used to determine the earthquake depth. Solutions from Chandra (1981, 1984) are not included in this compilation, as the sparse distribution of polarity data and small size of many of the earthquakes suggests that these solutions may not be reliable (Jackson & McKenzie 1984).

Where no manually processed solution, either from body-waveform modelling or first motions, is available, earthquake focal mechanisms are taken from the gCMT catalogue (Dziewonski

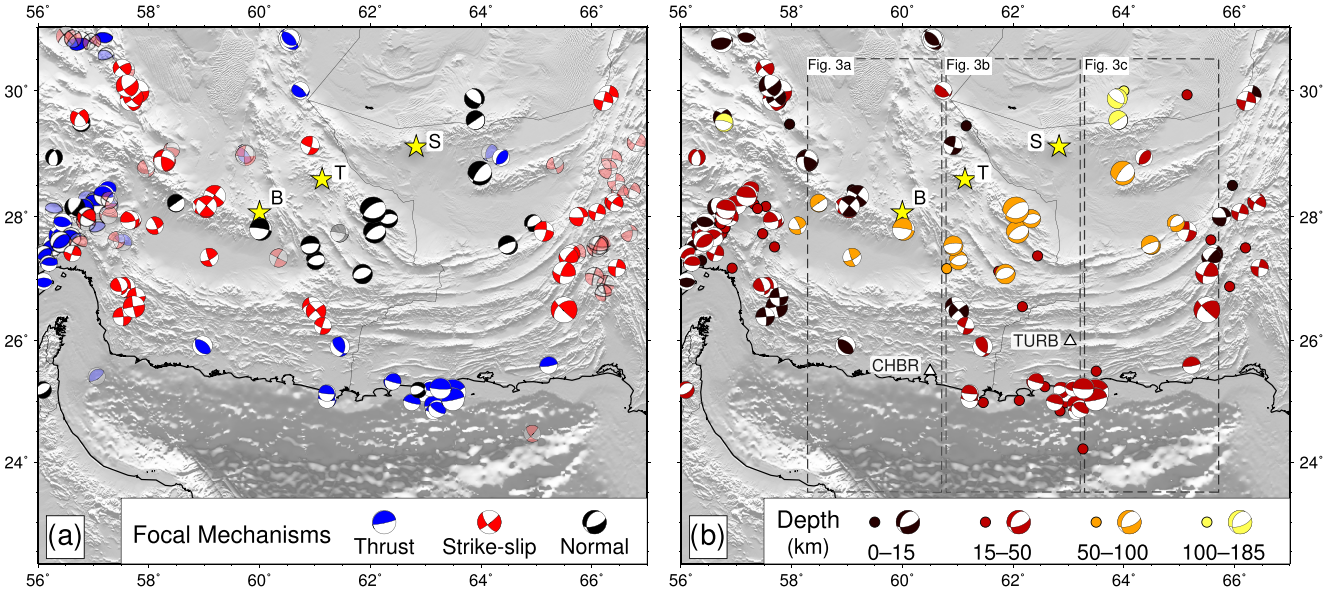

Figure 2. (a) All earthquakes, $m_b > 4$, from 1945–2013 with focal mechanisms reported by gCMT or in the literature (see Section 2.1 for citations) and the M_w 6.3 2017 February 7 earthquake, which was a shallow thrust in the cluster near the Pakistani coast. Events for which we consider the depth and/or focal mechanism to be poorly constrained are shown as semi-transparent. Focal mechanisms are coloured by rake, as shown in the key. Blue: thrust earthquakes, red: strike-slip earthquakes and black: normal-faulting earthquakes. Note the spatial separation of mechanisms; shallow thrusts cluster at the coastline and strike-slip events are concentrated at the eastern and western edges of the accretionary prism. (b) Earthquakes, $m_b > 4$, from 1945–2013 with well-constrained depths, as described in Section 2.1. Where well-constrained focal mechanisms are available (from body-waveform modelling, first motions or gCMT solutions with >70 per cent double-couple) these are coloured by depth, as shown in the key. Earthquakes with well-constrained depths but no mechanism are plotted as circles, with the same colour scale. Dashed boxes show the region in which earthquakes are projected on to each of the profiles in Fig. 3. White triangles show the locations of seismometers, CHBR and TURB. In (a) and (b), B, T and S are the volcanic centres Bazman, Taftan and Sultan.

et al. 1981; Ekström *et al.* 2012) and hypocentral locations from the EHB catalogue (Engdahl *et al.* 1998), up to the beginning of 2009, and the ISC (International Seismological Centre 2015), from 2009 onwards. The EHB catalogue for Iran was reviewed up to 2004 by Engdahl *et al.* (2006), and the earthquake locations given in that review are used in preference to the original catalogue. For these earthquakes a well-constrained depth means that the hypocentre was calculated using more than five depth phases and at least 50 stations, with the depth free to change in the inversion. Our results would not change substantially for small variations in these cut-offs, which have been chosen based on the experience of previous authors (e.g. Jackson 1980; Engdahl *et al.* 1998). With these constraints, we expect the errors in EHB/ISC locations to be 10–15 km in epicentre and ∼10 km in depth (Engdahl *et al.* 2006). We view a catalogue focal mechanism as well-constrained if it has a gCMT solution which is at least 70 per cent double couple, as defined by Jackson *et al.* (2002). Earthquakes shown as circles in Fig. 2(b) have well-constrained depths but no reliable focal mechanism. By using only well-constrained earthquake depths we are able to improve the model for the geometry of the subduction interface proposed by Frohling & Szeliga (2016), which is based on interpolation of the ISC catalogue, without quality control or body-waveform modelled events.

2.2 Receiver functions

Further constraints on the location and depth of the subduction interface can be provided by receiver-function analysis. We used data from two broad-band seismometers in the Makran: CHBR located at Chabahar in southern Iran and TURB located at Turbat in southern Pakistan (Fig. 1), which we use to determine teleseismic *P*-wave receiver functions (Fig. C1). We model these receiver functions simultaneously with surface waves to generate shear-wave velocity (Vs) profiles for each site. This joint-inversion technique has been used extensively by other authors (e.g. Julià *et al.* 2003; Dugda *et al.* 2007; Priestley *et al.* 2008) and is described in detail in Julià *et al.* (2000). A summary of these methods is provided in Appendix C. The shear-wave velocity profiles beneath both CHBR and TURB (red lines in Figs 3a and b) show a thick, low-wave-speed (∼3 km s^{-1}) layer, probably corresponding to the sediments of the accretionary wedge, overlying a high-wave-speed (∼4.1 km s^{-1}) basement, which we interpret as the top of the oceanic crust. This velocity increase occurs at 28 ± 2 km at TURB and 26 ± 2 km at CHAB. This increase in velocity is consistent with the location of the subduction interface inferred from earthquake locations (Fig. 3, see the discussion below).

2.3 Interpretation of subduction interface geometry

Fig. 3 shows three N–S profiles through the Makran, marked on Fig. 2(b), plotting only those events with well-constrained depths. These profiles have several important features. First, shallow thrust earthquakes on the subduction interface cluster around 62°E (Fig. 3b), just west of the proposed rupture area for the 1945 earthquake (Byrne *et al.* 1992). These events may be late-stage aftershocks of the 1945 earthquake, as aftershock sequences have been known to continue for decades or even centuries after the main shock (Ebel *et al.* 2000). Taking the fault planes of the shallow thrust earthquakes to be the northward-dipping nodal planes, most have dips of 8°–10° with an estimated error of ±5°. If these earthquakes occurred on the subduction interface, the dips of their nodal planes provide an estimate of the dip of that interface close to the

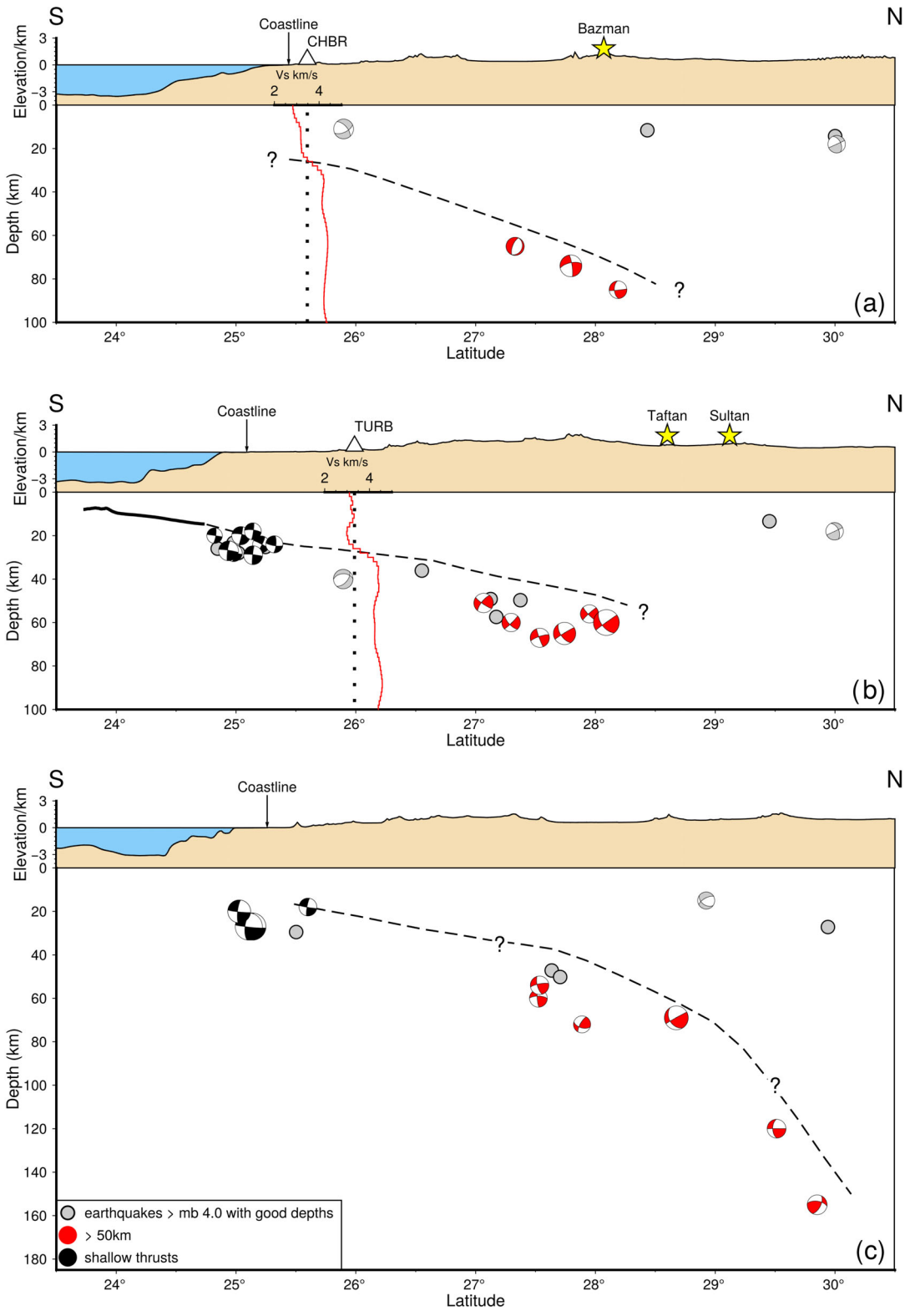

Figure 3. N–S profiles through the Makran showing earthquakes with well-constrained depths. Black focal mechanisms are shallow thrusts likely to be on, or close to, the subduction interface. Note that these thrusts cluster near the coastline. Red focal mechanisms are earthquakes with depths greater than 50 km which we interpret as occurring within the Arabian slab. Other earthquakes are shown in grey, with well-constrained focal mechanisms if available. Dashed lines show a possible geometry for the subduction interface in each profile, based on the data shown in this figure. The depth scale is the same in each profile. (a) Profile at 59.5°E. The red line shows the shear wave velocity profile at CHAB from joint inversion of receiver functions and surface waves. (b) Profile at 62°E. The solid black line is the basement reflector observed by Kopp *et al.* (2000), which is collinear with the earthquakes which we interpret as occurring on the subduction interface. The red line shows the shear wave velocity profile at TURB from joint inversion of receiver functions and surface waves. (c) Profile at 64.5°E. The deepest events in the Makran have been recorded near the location of this profile, providing the main constraints on the shape and location of the subduction interface north of the line of deep normal-faulting earthquakes (Fig. 2, Section 2).

coastline. Taking the surface projection of the interface as 24°N, where we observe a break in the bathymetric slope (white dashed line, Fig. 1), a line projected through the locations and depths of these earthquakes give an average subduction-interface dip of 6°–15°, consistent with the nodal-plane dips. This line is in very similar to the sediment-basement interface proposed by Kopp *et al.* (2000; bold line in Fig. 3b).

Another important feature of the earthquake distribution is a series of normal-faulting earthquakes at depths greater than 50 km. These earthquakes have an ∼ENE–WSW linear distribution in map view (black focal mechanisms in Fig. 2a), parallel to the strikes of their nodal-planes, and are observed across the longitudinal extent of the subduction zone. The dip of the seismogenic zone, which we infer from the earthquake distribution (dashed line, Fig. 3c), appears to steepen to the north of this line of earthquakes. We therefore suggest that these normal-faulting earthquakes may represent extension at a hinge in the subducting Arabian plate, as has been suggested in other subduction zones with variable dip (Isacks & Barazangi 1977).

Volcanic arcs were thought to form approximately above the 100 km contour of subducting slabs (Davis *et al.* 1983) but significant variations have been found (e.g. England *et al.* 2004; Syracuse & Abers 2006), probably due to the dependence of thermal structure on convergence rate, plate dip and age (England & Wilkins 2004). Our proposed hinge line lies just south of the volcanic arc in the Makran. This arc is composed of three main volcanic centres (yellow stars in Figs 2 and 3), which have chemical signatures indicative of subduction volcanism (Biabangard & Moradian 2008; Nicholson *et al.* 2010; Saadat & Stern 2011). Earthquakes deeper than the proposed hinge line have only been recorded in the east (with the exception of an isolated deep event in the far west, reported by Maggi *et al.* 2000), within the region profiled in Fig. 3(c), making it difficult to constrain the depth of the subduction interface beneath the arc. However, one of the normal-faulting earthquakes occurred almost directly beneath Bazman volcano, at a depth of 74 km (Jacob & Quittmeyer 1979). This suggests that the subduction interface is no deeper than ∼80 km under this part of the volcanic arc, allowing for ±5 km possible error in the earthquake depth. For the subduction interface to reach a depth of ∼100 km by the latitudes of Taftan and Sultan (at 62°E) it would need to significantly increase its dip north of the line of normal-faulting earthquakes. This geometry is consistent with our interpretation of these earthquakes as representing extension at a hinge in the subducting plate. Since these normal-faulting earthquakes occur within the descending slab, they provide an upper limit on the average dip of the subduction interface between their locations and the trench. We find maximum average dips of ∼11° in the western Makran, ∼9° in the central region and ∼8° in the eastern Makran.

The uncertainties in our estimates of the dip of the subduction interface do not allow us to definitively identify lateral variations in the geometry of the subduction interface. However, the slight decrease in our estimates of maximum average dip from west to east is consistent with the volcanic centres in the east being further north than those in the west (Byrne *et al.* 1992). The contrast in deep seismicity between the east and west is also unclear. From our profiles (Fig. 3) it might appear that the only earthquakes deeper than 100 km have occurred in the eastern Makran. However, the deep event in the western Makran, mentioned above, which does not lie within the area of our profiles, was suggested by Maggi *et al.* (2000) to have occurred in the subducting Arabian plate (Fig. 2b at ∼57 E, 29 N). More earthquake observations will be needed in order to resolve any lateral variations.

3 ELASTIC STRAIN ACCUMULATION ON THE SUBDUCTION INTERFACE

The absence of shallow thrust earthquakes in the western Makran, discussed above, does not necessarily imply that the subduction interface in the western Makran is not locked and accumulating elastic strain. We use published GPS velocities over ∼15 yrs from the Iranian Makran (marked with white squares in Fig. 1; Bayer *et al.* 2006; Masson *et al.* 2007; Peyret *et al.* 2009; Walpersdorf *et al.* 2014; Frohling & Szeliga 2016), to determine whether the subduction interface in the western Makran might be locked. We also include velocity estimates from two sites in the onshore part of the prism (ANGN and NKSR) which have not previously been published. These sites form part of the Iranian national network of GNSS receivers maintained by the National Cartographic Centre, Tehran and are equipped with Ashtech UZ-12 ICGRS receivers with choke-ring antennae, mounted on concrete pillars. Data were recorded continuously from August 2011 to February 2013 and processed using the GAMIT/GLOBK software, version 10.4 (Herring *et al.* 2010). Time-averaged linear velocities for these sites are estimated by applying the GLOBK Kalman filter to the daily solutions.

We apply the backslip technique proposed by Savage (1983) to a planar fault in an elastic half-space and use Okada's (1985) equations to model the surface velocities resulting from different locking depths and subduction-interface positions. We then compare these model predictions with velocities measured by GPS. Subduction zones are not normally locked to depths greater than 40 km, measured vertically from the surface (Tichelaar & Ruff 1993; Hyndman *et al.* 1997; Lay *et al.* 2005; Bouchon *et al.* 2016; Ye *et al.* 2016) and our profiles in Fig. 3 show that a planar interface is a reasonable assumption at these shallow depths. Frohling & Szeliga (2016) investigated the coupling of the Makran using a similar backslip approach but with a more complex model for the subduction interface. However, as discussed in Section 2, those authors did not apply quality control to the earthquakes used to infer the position and shape of the subduction interface, which is, in any case, poorly constrained. We therefore consider a planar model of the interface to be more appropriate for this modelling. We also use GPS velocities not incorporated into Frohling & Szeliga's (2016) modelling, in order to provide more realistic constraints on the degree of locking on the subduction interface.

The uncertainties in the position and shape of the subduction interface make the choice of model parameters difficult. The overall rate of convergence is also poorly constrained due to the scarcity of GPS stations in the region (Vernant *et al.* 2004). Inverse methods are therefore inappropriate for analysing the degree of coupling as the inversions are very underdetermined. Instead, we calculate forward models for end-member combinations of parameters and a selection of intermediate values. The aim of this modelling is to ascertain whether coupling in the western Makran, to a geologically reasonable depth, on an interface consistent with our results from earthquakes and receiver functions, is consistent with the observed GPS velocities, rather than to determine the actual pattern of coupling on the subduction interface, which is not possible with the data which is currently available.

Since we are considering a planar interface, we must specify the average dip of the megathrust. We take 6° as the minimum dip based on the locations and depths of the shallow thrust earthquakes in Fig. 3(b), which are likely to have occurred on the subduction interface (Section 2.3). The depths of normal-faulting earthquakes associated with the bending of the Arabian slab, due to the increase in dip of the subduction interface (Section 2.3), provide an upper

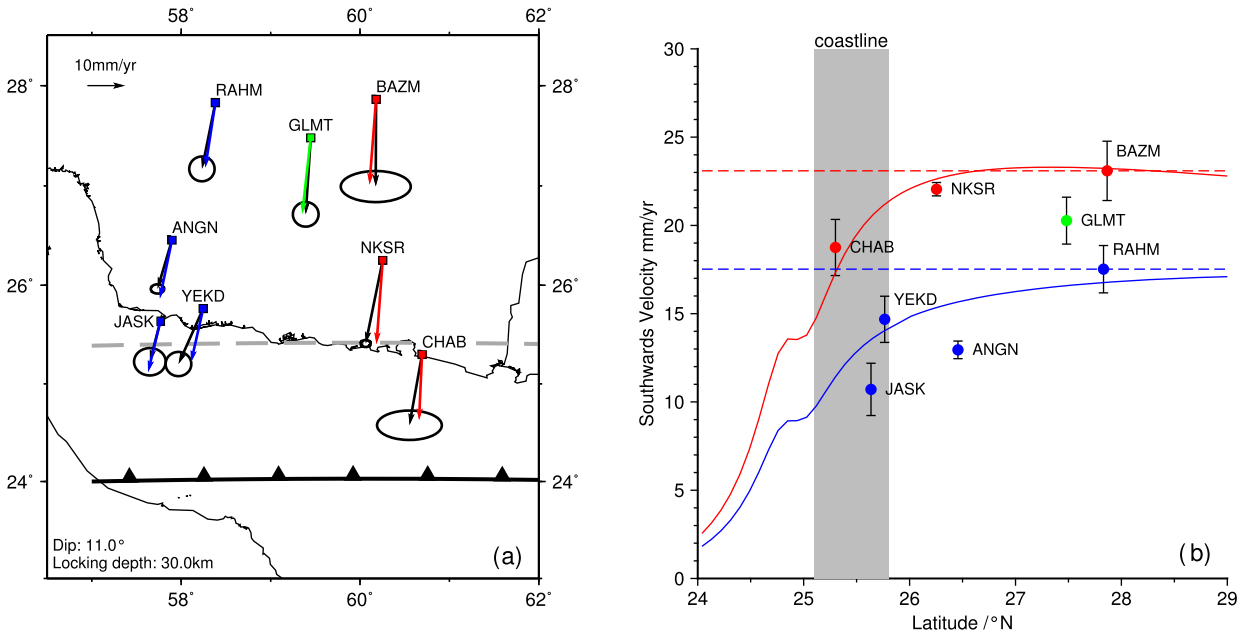

Figure 4. (a) Black arrows show published GPS velocities (sources as in Fig. 1) and those presented in this paper (ANGN and NKSR), with 95 per cent confidence ellipses. Coloured arrows are predictions of surface velocity from a coupling model with a locking depth of 30 km, mean dip of 11° and overall convergence rates of 20.4 and 32.6 mm yr^{-1} west and east of 59.5°E, respectively. Model predictions at western stations are shown with blue arrows, at eastern stations with red arrows and at station GLMT, which is centrally positioned within the region, with a green arrow. The surface projection of the subduction interface in this model is shown by the black-toothed line and the location of the down-dip limit of locking is shown by the grey-dashed line. (b) N–S profiles through surface velocities. Circles show the southwards component of published GPS velocities and those presented in this paper, with their associated errors. Those stations in blue are located west of 59.5°E. Those stations in red are located east of 59.5°E. Solid lines are profiles at 58°E (blue) and 60.5°E (red) through the surface velocities resulting from the model in (a). Dashed lines show profiles of constant surface velocity, at the velocities of the northernmost GPS stations (red at BAZM, blue at RAHM). Station GLMT lies at approximately 59.5° and is coloured green. The grey bar shows the location of the coastline across the region.

bound on the average dip of the interface, since they must lie within the subducting slab. There is a trade-off between the estimated maximum dip and the choice of the surface projection of the subduction interface but, by taking the most northerly possible surface projection, we ensure that this approach gives an upper bound on the range of possible dips. We find that the maximum possible average dip in the shallow (<40 km) part of the slab is ∼11° (see Section 2.3).

Although there is no clear bathymetric trench in the Makran, due to the high sediment input (White & Louden 1982; Laane & Chen 1989), the slope break at the toe of the accretionary wedge is visible in the bathymetry and lies at ∼24°N (white dashed line, Fig. 1). We use this slope break as a proxy for the surface projection of the subduction interface, which we vary between 23.5°N and 24.5°N to allow for errors in its location. We allow the locking depth to vary between 0 km, a freely sliding interface, and 40 km, which is the maximum depth to which subduction interfaces are normally locked (Tichelaar & Ruff 1993; Hyndman *et al.* 1997; Lay *et al.* 2005; Bouchon *et al.* 2016; Ye *et al.* 2016). The ∼150 km distance between the slope break and the coast means that the GPS data are not sensitive to very shallow variations in locking depth.

The overall convergence rate is varied in our calculations in order to reproduce the observed velocities. The western stations (YEKD, ANGN, RAHM, blue in Fig. 4) require a lower overall convergence rate than those to the east (CHAB, NKSR, BAZM, red in Fig. 4) in order to match their velocities. This is consistent with the Arabia–Eurasia convergence rate increasing from west to east across the region. Additionally, the western stations are near the western edge of the subduction zone, which may account for their lower velocities. To allow for this velocity variation, in our calculations we use two adjoining megathrust planes with the same geometry, but with different rakes (slip directions) and slip rates. Our calculated surface velocities are the result of locking on both these planes. The GPS station GLMT lies at an intermediate longitude, where the parameters of both planes contributes to the surface deformation.

We find that there are multiple parameter combinations that result in reasonable agreement between the observed and synthetic surface velocities. Fig. 4(a) shows an example of one such model in map view, in which the locking depth is 30 km, the dip is 11° and the convergence rates in the western and eastern regions are 20.4 mm yr^{-1} and 32.6 mm yr^{-1} respectively. This model has an RMS misfit of 1.7 mm yr^{-1}, similar to the resolution of the GPS measurements. Fig. 4(b) shows two profiles through the southwards component of the surface velocities from this model, at 58°E and 60.5°E, showing the faster velocities of the more easterly stations. Fig. 4(b) also shows that the surface velocities which would result from a plate interface sliding freely at the velocity of the northernmost GPS stations (dashed lines) are unable to reproduce the observed velocities near the coastline. While the precise geometry of locking on the interface cannot be resolved with this data set, the decrease in velocities towards the coast does require locking to some depth, or internal deformation within the wedge (e.g. Haghipour *et al.* 2012), which is not accounted for in the backslip approach. We cannot distinguish between these possibilities using the GPS data alone, and internal deformation may make a contribution. Haghipour *et al.* (2012) suggest a shortening rate of 0.8–1.2 mm yr^{-1} between the coast and ∼26.5°N in the Iranian Makran, based on ^{10}Be exposure dating and structural measurements of fluvial terraces. However, this shortening is not enough to account for all of the compression we observe, suggesting that elastic strain accumulation above a locked megathrust does play a role. We are also encouraged in our

interpretation by observations in other subduction zones, such as Sumatra, where earthquakes are inferred from the palaeogeodetic record to have occurred historically in regions which GPS measurements suggest are accumulating elastic strain at the present day (Natawidjaja *et al.* 2004; Chlieh *et al.* 2008; Konca *et al.* 2008).

Our modelling shows that a locked subduction interface in the western Makran is consistent with measured GPS velocities. This corroborates suggestions from observations of tsunami deposits and tsunami modelling (Hoffmann *et al.* 2015) that the western Makran megathrust may be seismogenic. If the whole along-strike extent of the megathrust were to rupture in single earthquake the subduction zone could be capable of generating an M_w 9 earthquake, as proposed by Smith *et al.* (2013), which has significant implications for earthquake and tsunami risk around the Arabian Sea.

4 SOUTHERN TERMINATION OF N–S STRIKE-SLIP FAULTING IN THE SISTAN SUTURE ZONE

The compression seen in the GPS data described above plays an important role in the deformation of the Makran, but right-lateral shear, resulting from differential motion between Central Iran and Afghanistan, is also key. How the N–S right-lateral strike-slip faulting in the SSZ (Fig. 1) is accommodated at the zone's southern end is a long-standing tectonic problem.

Jackson & McKenzie (1984) proposed a solution to this problem involving an Euler pole for the motion of Central Iran relative to Eurasia that is close to the southern end of the SSZ, so that there is very little motion to accommodate between Eurasia and Central Iran in the south. The slip on the faults within the SSZ would then die out towards their southern ends. However, this suggestion is not compatible with recent GPS measurements (Vernant *et al.* 2004; Walpersdorf *et al.* 2014). Alternatively, Byrne *et al.* (1992) argued that two strike-slip earthquakes on 1979 January 10 (at 61°E, 26.5°N on Fig. 2b) indicate that right-lateral faulting does continue across the prism. However, there is no evidence of significant right-lateral offsets in the geology or geomorphology of the Makran ranges. The total offset of the SSZ is suggested to be at least 70 km, based on offset units in the Neh complex (north of Fig. 1; Tirrul *et al.* 1983; Walker & Jackson 2004), which would result in visible geological offsets if this motion continued through the accretionary wedge. Additionally, these events, which are the largest of three strike-slip events which have been observed in the central Makran, were M_w 5.8 and 5.9, accounting for only a year's worth of strain accumulation at the slip rates proposed for the SSZ (Section 4.2). It is also not known which nodal planes are the fault planes for these two earthquakes. Kukowski *et al.* (2000) proposed a new plate-boundary strike-slip fault, the Sonne fault, separating the Arabian plate from the Ormara microplate (their Fig. 3), with morphological expression in the accretionary prism due to high coupling. Lin *et al.* (2015) suggested that this fault might be a continuation of the SSZ. However, the proposed Sonne fault, the existence of which is in any case unclear since it is not observed to offset structures in the forearc in seismic reflection surveys (Smith *et al.* 2013), is suggested to be left-lateral (Kukowski *et al.* 2000), whereas the SSZ is right-lateral. How the right-lateral shear across the SSZ is accommodated at the zone's southern end is thus an open question, to which we discuss three possible solutions. In the following discussion we consider a range of rates of right-lateral shear across the SSZ of 5–15 mm yr^{-1}. The present day rate of shear is 5.6 ± 0.6 mm yr^{-1} (Walpersdorf *et al.* 2014), but we use a high upper bound to allow for uncertainty in the long-term rate.

One possibility is that the right-lateral faults terminate in thrusts with decreasing slip towards their ends (Fig. 5a), similar to those observed in Mongolia (Bayasgalan *et al.* 1999a). Strike-slip faults terminate in thrust faults at the northern end of the SSZ and these thrusts can move in earthquakes, either concurrently with strike-slip motion, for example, the 1997 Zirkuh earthquake (Berberian *et al.* 1999), or in dominantly thrust earthquakes, for example, the 1994 Sefidabeh earthquakes (Berberian *et al.* 2000). The assumption that the faults of the SSZ terminate in thrusts is implicit in much of the literature (e.g. Haghipour & Burg 2014) but its kinematic implications have not been fully considered in previous studies.

A second possibility is that the right-lateral N–S shear, accommodated by the faults of the SSZ, is transferred onto left-lateral E–W striking faults in the Makran accretionary prism (Fig. 5b). Left-lateral E–W striking faults can accommodate right-lateral N–S shear by rotating clockwise about vertical axes (e.g. McKenzie & Jackson 1986). Such vertical-axis rotations accommodate some of the right-lateral shear at the northern end of the SSZ, for example on the Dasht-e-Bayaz fault (Walker *et al.* 2004), and have been reported at the western margin of the Makran (Penney *et al.* 2015).

A final possibility is that the right-lateral motion of the SSZ is transferred onto the faults of the Minab-Zendan-Palami (MZP) fault zone (Fig. 1) and nearby strike-slip faults (Penney *et al.* 2015), which, combined, accommodate ∼17 mm yr^{-1} of right-lateral shear (Peyret *et al.* 2009). Geometrically, this scenario requires the Jaz Murian depression to be bounded by normal faults (Fig. 5c). We consider each of these three possibilities in turn.

4.1 Thrust faulting

For the faults of the SSZ to terminate in thrusts (Fig. 5a), the northern part of the Makran prism, immediately south of the Mashkel depression (Fig. 1), would need to accommodate shortening. Recently published GPS velocities from Frohling & Szeliga (2016) show a difference of 2 mm yr^{-1} in southwards velocities relative to Arabia between DALN and PANG at 28.89°N and 26.98°N (Fig. 1). This velocity difference is within the stations' formal combined error. Any shortening is therefore small relative to the combined slip rate of the faults in the SSZ (5–15 mm yr^{-1}, e.g. Walpersdorf *et al.* 2014; Walker & Jackson 2004). Additionally, no shallow thrust earthquakes have been recorded along the southern margin of the Mashkel depression from 1945–2013 (Figs 2a and b). Taken alone this would be insufficient to rule out the possibility of shortening across the back of the prism as the repeat times of earthquakes might be longer than our records. However, the absence of thrust earthquakes is consistent with the lack of shortening seen in the GPS data, suggesting that this method of termination of the strike-slip motion in the SSZ is unlikely.

4.2 Vertical-axis rotations

A velocity field equivalent to right-lateral shear can be accommodated by left-lateral motion on perpendicularly oriented planes, combined with clockwise rotation about vertical axes (e.g. Freund 1970; McKenzie & Jackson 1986; Nur *et al.* 1986). The right-lateral shear on the N–S striking faults of the SSZ could thus be transferred on to E–W striking left-lateral faults in the Makran accretionary prism (Fig. 5b). Since the trends of folds in the prism

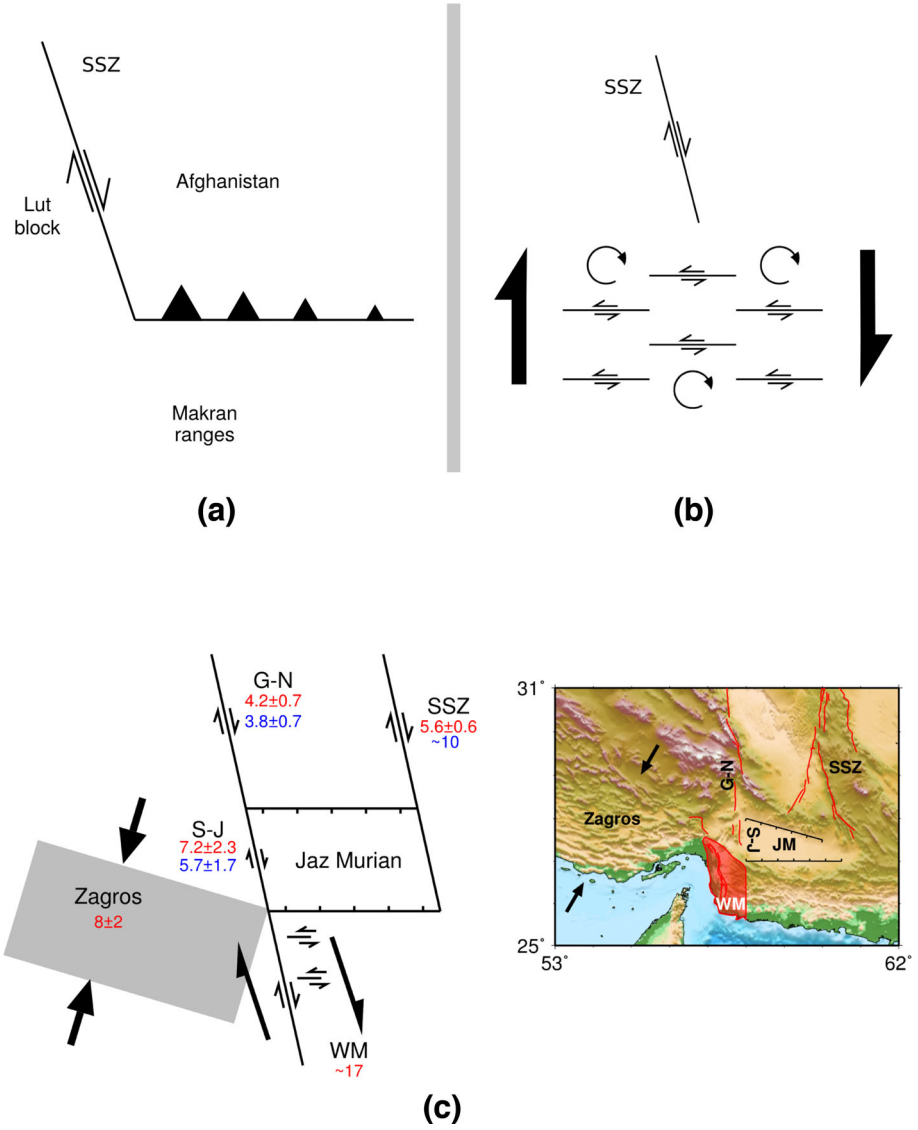

Figure 5. Possible methods of accommodating right-lateral motion at the southern end of the SSZ. (a) Right-lateral ~N–S faults terminate in E–W thrusts with displacements dying out towards their ends (toothed line). (b) Right-lateral motion on ~N–S striking faults is transferred on to E–W striking left-lateral faults, which rotate clockwise about vertical axes. (c) Left: Right-lateral motion on the ~N–S striking faults in the SSZ is transferred to the western Makran (WM) by normal faults bounding the Jaz Murian depression (JM). G-N and S-J are the Gowk-Nayband and Sabzevaran-Jiroft fault systems. Numbers are present day (red) and Quaternary (blue) rates in mm yr^{-1} (Walker *et al.* 2004; Regard *et al.* 2005; Walpersdorf *et al.* 2006; Peyret *et al.* 2009; Walker *et al.* 2010; Walpersdorf *et al.* 2014). Right: relationship to topography - red lines are faults as in Fig. 1.

are E–W we would not necessarily expect to easily observe large geological offsets as a result of such faulting.

Tirrul *et al.* (1983) used offset units within the Neh complex (north of Fig. 1) to suggest at least 60 km of cumulative motion on the Neh fault system, one of the systems of N–S striking, right-lateral faults within the SSZ, since the Pliocene (~5 Ma, see also Tirrul *et al.* 1980). Walker & Jackson (2004) found that the cumulative offset across the SSZ, combining offsets across the multiple active faults, is at least 70 km over the same time period. Walker & Jackson (2004) suggested that the cumulative offset may be as much as 105 km, if the right-lateral faults have been slipping at 15 mm yr^{-1} over the last 7 Ma, an upper bound on both the current slip rate (Vernant *et al.* 2004) and the duration of the current faulting configuration (Allen *et al.* 2004). These offset estimates give a long-term slip rate on the SSZ of 10–21 mm yr^{-1}. The present-day GPS slip rate is 5.6 ± 0.6 mm yr^{-1} across all of the faults in the SSZ (Walpersdorf *et al.* 2014, referred to collectively by those authors as the 'East Lut' fault). Walker & Jackson (2004) discussed the problem of reconciling these rates, and the uncertainties in the long term slip rates due to uncertainty about the duration of the current configuration of faulting. The lower short term rate may indicate that the proposed long term slip rates are overestimates, or that the rate of motion has changed. To reflect this uncertainty, in the following calculations we have used total slip rates on the faults in the SSZ of 5–15 mm yr^{-1} and cumulative offsets of 70–105 km, in order to encompass the full range of possibilities.

Here we quantify the amount of rotation which would be required in the Makran to accommodate the offset on the strike-slip faults in the SSZ, and relate this to seismological and structural observations. Using the geometry shown in Fig. D1, we calculate the slip rate required on left-lateral faults bounding blocks of given length and width in order to accommodate a particular total slip rate on

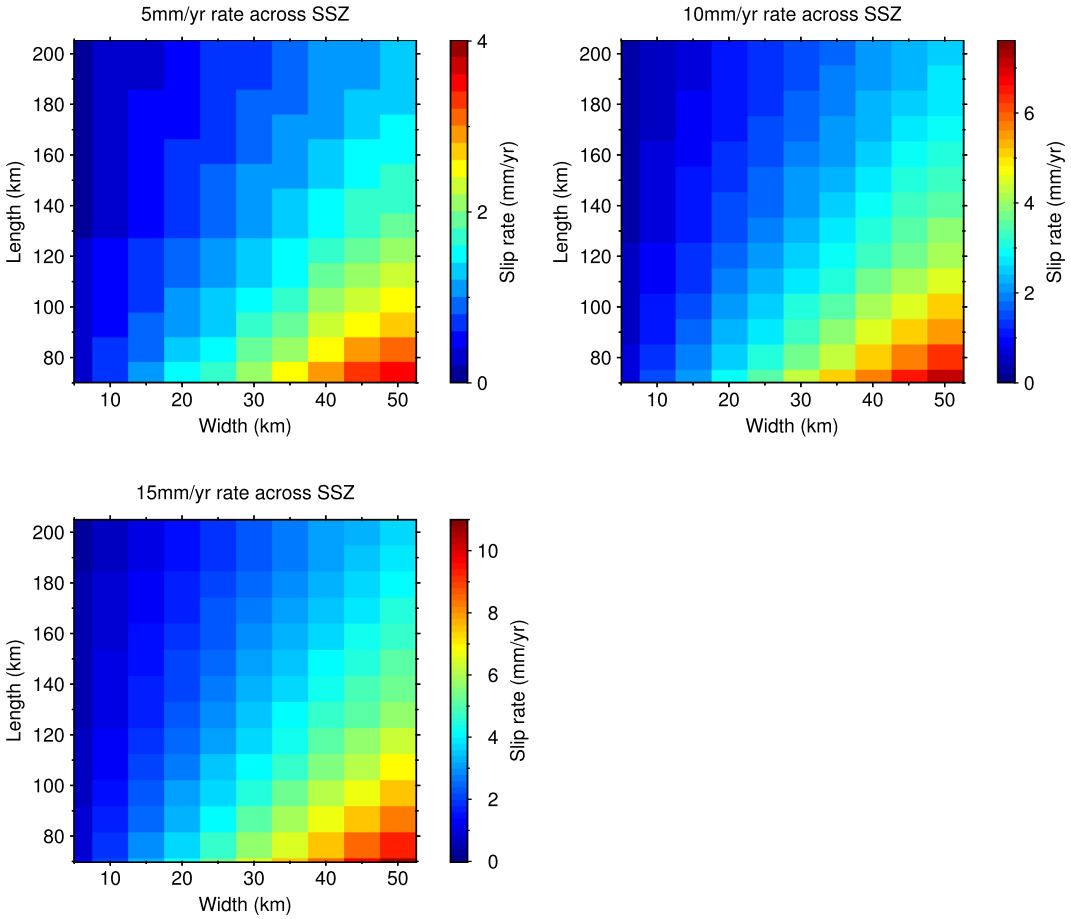

Figure 6. Slip rates required on E–W striking left-lateral faults bounding blocks of given length and width in order to accommodate a particular slip rate on the N–S striking right-lateral faults in the SSZ. The assumed slip rate on these right-lateral faults is given at the top of each plot. Note that the colour scale for the slip rate is different for each plot.

the N–S strike-slip faults in the SSZ. The results of this calculation are shown in Fig. 6. We then use the calculated slip rates on these left-lateral faults to estimate the seismic moment accumulated per year. This requires us to assume a down-dip fault extent, which we take as 20 km (Fig. 3). Although the fault length appears in the expression for seismic moment, Appendix D1 shows that, since the fault length is much greater than the time-averaged annual slip, the seismic moment is independent of fault length to first order. We find that the accumulated moment, at the 10 mm yr^{-1} slip rate suggested by Walker & Jackson (2004), is 1.5×10^{18} Nm yr^{-1}. This moment is equivalent to an M_w 7 earthquake every 21 yr or an M_w 8 every 670 yr, and is independent of block width (Appendix D1). Even for the lower, GPS-derived slip rate of ∼5 mm yr^{-1} the accumulated moment is 9×10^{17} Nm yr^{-1}, equivalent to an M_w 7 earthquake every 34 yr. The M_w 5.8 and 5.9 earthquakes described by Byrne *et al.* (1992) are the largest examples of strike-slip faulting near the centre of the onshore prism, equivalent to less than a year's worth of moment accumulation for a cumulative slip rate on the faults in the SSZ of 10 mm yr^{-1}, or less than two years' worth for a rate of 5 mm yr^{-1}. However, a lack of observed left-lateral strike-slip earthquakes does not necessarily imply that such earthquakes do not occur, since the repeat time of such earthquakes may be longer than the time covered by our records.

Next, we consider the total angle through which blocks bounded by left-lateral faults would need to rotate in order to accommodate a cumulative, right-lateral offset of 70–105 km on the N–S strike-slip faults in the SSZ. The results are shown in Fig. 7(a). We use the same geometry (Fig. D1) as above but replace the slip rate on the strike-slip faults in the SSZ with the cumulative right-lateral offset across the zone. We find that the minimum angle through which the left-lateral faults would need to have rotated is ∼20°. Such rotation should be visible as a variation in the trends of structures across the central part of the onshore prism, and in palaeomagnetic studies. Conrad *et al.* (1981) found that magnetization directions of recent volcanics (less than 10 Myr) are close to the present-day magnetic field, suggesting that no significant rotation has occurred in the last 10 Myr.

Fig. 7(b) shows a map of structural trends in the Makran. There is a deviation of the structural trends in the west of the subduction zone, in the region where vertical-axis rotations have previously been reported (white-shaded area in Fig. 1; Penney *et al.* 2015), but further east there is no systematic variation in structural trends across the central Makran region. This observation, combined with our calculations, suggests that right-lateral shear at the southern end of the SSZ is not accommodated by vertical-axis rotations within the Makran accretionary prism.

4.3 The Jaz Murian depression as an extensional basin

The right-lateral shear across the SSZ could be transferred to the right-lateral shear zone at the western edge of the Makran

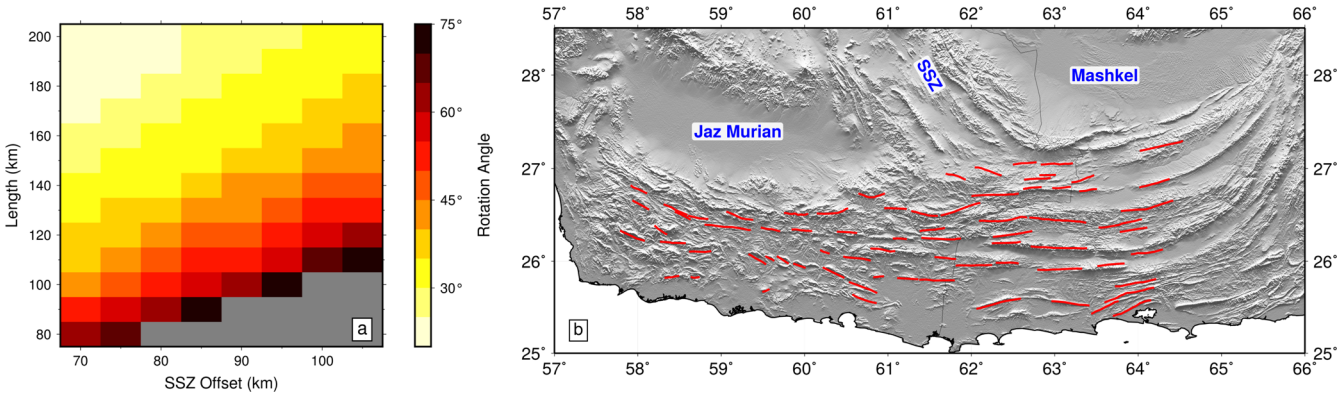

Figure 7. (a) Plot of the cumulative angle through which blocks, of given length, bounded by left-lateral faults would need to have rotated clockwise in order to accommodate the total right-lateral offset across the SSZ. The minimum rotation required is ∼20°. Left-lateral faults shorter than the total offset across the SSZ cannot accommodate the offset by rotation; this part of the plot is shaded in grey. (b) Map of the Makran accretionary prism with structural trends (from fold axes and bedding planes identified on satellite imagery) marked as red lines. There is no evidence of systematic vertical-axis rotations in the central section of the prism.

accretionary prism, marked 'WM' in Fig. 5(c). This geometry is similar to that of a releasing bend, requiring the Jaz Murian depression to be bounded by extensional faults.

We first consider how such a transfer of motion would work kinematically, by looking at the slip rates of the fault systems in the region. We then examine the geomorphology and geology of the basin to determine whether the Jaz Murian depression is bounded by active faults and, if so, what the sense of motion on these faults is. Finally, we use our results from Section 3 regarding the degree of coupling on the subduction interface in the western Makran in order to discuss whether the measured GPS velocities are consistent with this kinematic model.

4.3.1 Slip rates

For the transfer of motion across the Jaz Murian to be kinematically plausible, the rate of right-lateral shear across the western Makran must be sufficient to accommodate the right-lateral motion on the Sabzevaran-Jiroft fault system to the north (S-J in Fig. 5c), shortening across the southeastern Zagros, and the right-lateral shear across the faults of the SSZ.

The present-day slip rate on the Sabzevaran-Jiroft fault system, at the western boundary of the Jaz Murian depression (Fig. 5c), has been estimated from GPS measurements to be 7 ± 2 mm yr^{-1} (Peyret *et al.* 2009). Walpersdorf *et al.* (2014) found a rate of 2.3 ± 2.4 mm yr^{-1} across only the Sabzevaran fault, but their result is probably an underestimate as the GPS stations used to assess the rate lie within the region likely to be affected by elastic deformation due to fault locking. The Quaternary slip rate across these faults has been found to be 5.7 ± 1.7 mm yr^{-1} (Regard *et al.* 2005), which is consistent with the GPS estimates. To the north the Sabzevaran-Jiroft faults connect with the Gowk-Nayband fault system (G-N in Fig. 5c). The southernmost fault in this system is the Gowk fault, which has comparable GPS and Holocene slip rates of 4.2 ± 0.7 mm yr^{-1} (Walpersdorf *et al.* 2014) and 3.8 ± 0.7 mm yr^{-1} (Walker *et al.* 2010). These rates are within error of those for the Sabzevaran-Jiroft system, but are slightly lower, allowing for the possibility of slow extension across the northern margin of the Jaz Murian depression. The rate of shortening across the southeastern Zagros is 8 ± 2 mm yr^{-1} (Walpersdorf *et al.* 2006). The best estimate of the present-day rate of shear across the faults in the SSZ is 5.6 ± 0.6 mm yr^{-1} (Walpersdorf *et al.* 2014).

GPS velocities at the western edge of the Makran show ∼17 mm yr^{-1} right-lateral shear between 56.7°E and 58.4°E (white-shaded area in Fig. 1; Peyret *et al.* 2009). This is accommodated by both the N–S striking faults of the Minab-Zendan-Palami fault zone (e.g. Bayer *et al.* 2006, MZP in Fig. 1) and left-lateral E–W striking faults to the east (Penney *et al.* 2015), which rotate clockwise about vertical axes. The total motion from shortening in the Zagros, right-lateral faults to the north in the Sabzevaran-Jiroft fault system, and the faults of the SSZ is ∼18 mm yr^{-1}, so the rate of right-lateral shear in the western Makran is sufficient to take up that motion. The agreement between these rates suggests that it is probable that the right-lateral shear across the SSZ is transferred to the western Makran by normal faulting at the boundaries of the Jaz Murian depression.

4.3.2 Geomorphology

We use a combination of SPOT (from Google Earth), Landsat and ASTER imagery, and SRTM topography, to look at the geomorphology of the Jaz Murian depression. The strike-slip faults at the western edge of the depression have very clear surface expressions (e.g. Morgan *et al.* 1979; Regard *et al.* 2005; Meyer & Le Dortz 2007). We concentrate on the northern and southern boundaries of the basin. A first-order feature of the depression morphology is its sharply defined edges, with large topographic contrasts which have long, linear sections (Fig. 8a). These are particularly clear on the southern edge of the basin (Figs 8a–d) and are indicative of dip-slip faulting. The faceted topography of the basin edges is also a common feature of fault-controlled range fronts. Some of the alluvial fans at the edges of the depression show breaks in slope which we interpret as scarps (e.g. Fig. 8c). It is common to see migration of fault activity away from the range front (e.g. Avouac *et al.* 1993; Bayasgalan *et al.* 1999b) and these scarps may be evidence of such migration, or of secondary faults adjacent to the main structure (e.g. Goldsworthy & Jackson 2001). There is, therefore, convincing evidence for the Jaz Murian depression being bounded by active dip-slip faults.

We now consider the sense of motion on these bounding faults. Thrust faults are very common in Iran and often have a clear geomorphological expression, even where they do not reach the surface or their scarps are not preserved (e.g. Berberian 1981). In particular, anticlines in alluvium are often diagnostic of thrust-faulting,

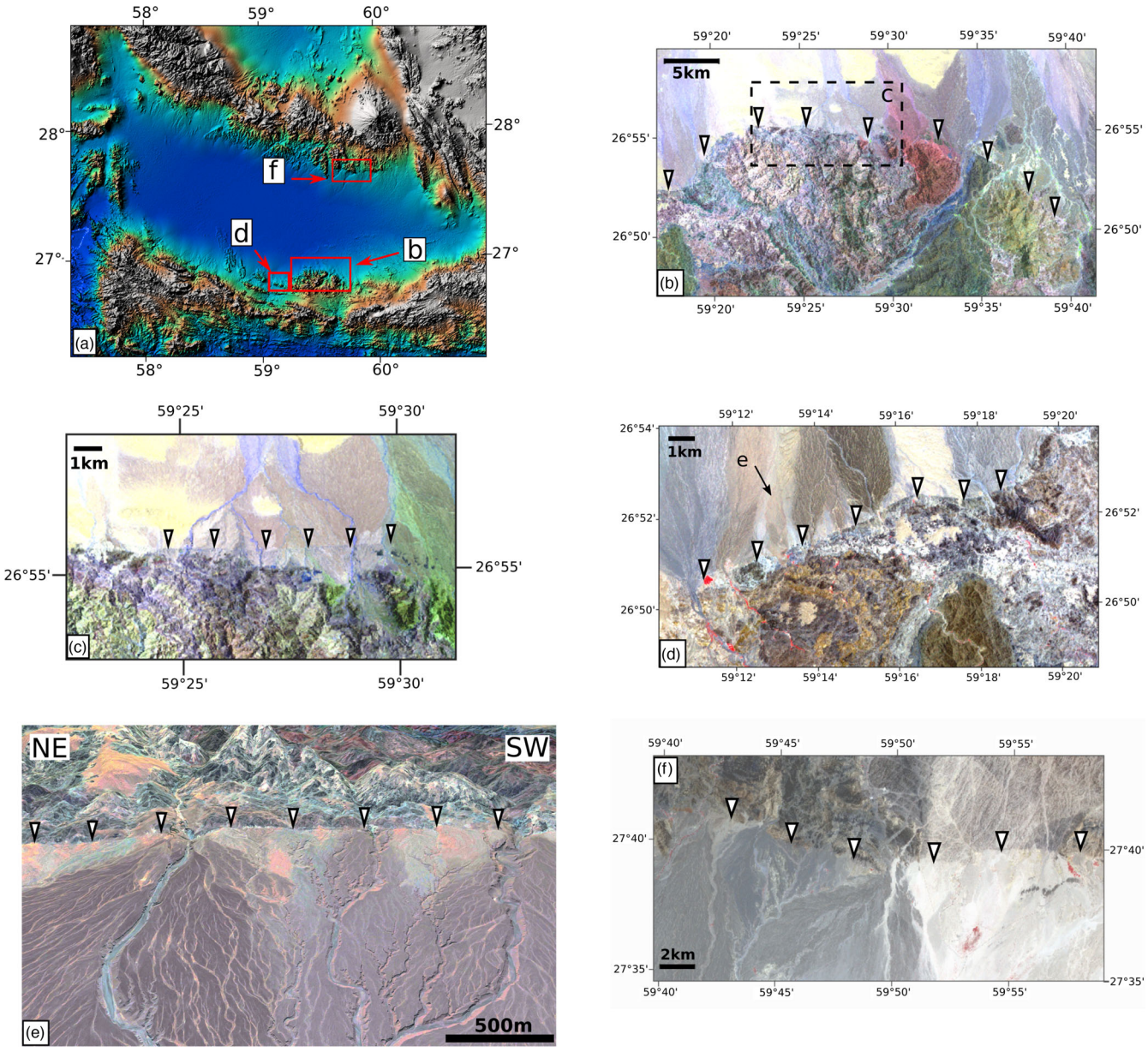

Figure 8. (a) SRTM topography of the Jaz Murian depression, shaded by elevation, showing locations of b, d and f. (b) Landsat TM image (bands 5, 4, 1 shown as R, G, B) of part of the southern edge of the Jaz Murian depression, location shown in (a). White arrows highlight the topographic discontinuity associated with the edges of the basin. (c) Landsat image (bands 7, 5, 1 as R, G, B), location shown in (b). A discontinuity in fan surfaces is picked out by the white arrows. (d) ASTER image (bands 3, 2, 1 as R, G, B), showing straight topographic discontinuity. Panel (e) shows the same discontinuity in Digital Globe imagery (©Google, ©DigitalGlobe, http://www.google.com/earth/) looking SE, along arrow marked in (d)). (f) ASTER image (spectral bands 3, 2, 1) of straight topographic discontinuity along the northern edge of the Jaz Murian. Note that the edge cuts the lithological contrast seen in the change from white to grey rocks.

and were seen to move in the Tabas and Sefidabeh earthquakes (e.g. Berberian *et al.* 2000; Walker *et al.* 2003). We do not see any evidence of such folding around the edges of the Jaz Murian depression. We see nothing in the geomorphology that is diagnostic of a particular sense of slip, although the lack of folding may be suggestive of normal faulting. Dolati (2010) and Haghipour *et al.* (2012) suggested that a series of normal faults run along the southeastern edge of the depression, based on structural mapping of serpentinites. The locations of these faults are consistent with our geomorphological observations of dip-slip faulting on the southern boundary of the Jaz Murian depression, and the faults are 10–20 km long so, if active, would break the entire seismogenic layer and be important for the regional tectonics. However, Dolati (2010) was not able to establish the timing of activity on these faults and it is therefore not clear whether the active deformation is also normal faulting.

4.3.3 *Temporal strain variations*

No shallow earthquakes with $m_b > 4.0$ have been reported on the northern or southern margins of the Jaz Murian depression between 1945 and 2013 (Fig. 2b), suggesting that if shallow extensional earthquakes occur they are likely to have a repeat time longer than our records. GPS velocities over the last 15 yr show compression

across the Jaz Murian depression (Peyret *et al.* 2009; Walpersdorf *et al.* 2014). However, this compression may be due to elastic strain accumulation above a locked megathrust. Whether this is the case depends on the degree of coupling on the subduction interface in the western Makran, which was discussed in Section 3. Recent studies in other subduction zones have reported time-varying strain in the overriding plate, linked to the megathrust earthquake cycle (e.g. Loveless *et al.* 2010; Arriagada *et al.* 2011; Aron *et al.* 2013; Baker *et al.* 2013; Scott *et al.* 2016). In the megathrust's interseismic period the overriding plate is in a compressional stress regime so normal-faulting earthquakes are suppressed and GPS signals indicate shortening. Immediately after a megathrust earthquake (perhaps even during the coseismic period; Hicks & Rietbrock 2015) compressive stresses in the overriding plate are reduced and normal-faulting earthquakes can occur. This temporal variation in the style of earthquakes has been observed extensively in Chile (e.g. Farías *et al.* 2011) and in Japan (e.g. Asano *et al.* 2011; McKenzie & Jackson 2012). Although the permanent extension associated with individual episodes of normal-faulting is small (Baker *et al.* 2013), over many earthquake cycles significant deformation could be accumulated. Such time-dependent deformation of the overriding plate requires the megathrust to be locked, accumulating elastic strain, and to move in earthquakes, rather than sliding continuously.

In Section 3 we showed that GPS data in the western Makran are consistent with the megathrust being locked. The absence of normal-faulting earthquakes on the bounding faults of the Jaz Murian depression, and the present-day compression seen in the GPS velocities, may, therefore, be due to compressive stresses and elastic strain accumulation in the overriding plate above a locked megathrust interface. This conclusion would be confirmed by the observation of normal-faulting earthquakes after an earthquake on the western Makran megathrust.

We conclude that it is likely that the Jaz Murian depression is bounded by E–W striking dip-slip faults, which are probably extensional. This normal-fault bounded basin may allow the right-lateral motion of the SSZ to be transferred on to the faults of the MZP and adjacent strike-slip faults as shown Fig. 5(c). Unlike vertical-axis rotations or thrusting at the back of the accretionary prism, such a transfer of motion provides a geologically plausible mechanism to transmit the right-lateral motion on the SSZ to the subduction zone, which is consistent with the present-day motions. This mechanism is viable because compression in the GPS velocities across the boundaries of the Jaz Murian depression may be due to locking on the subduction interface.

5 DYNAMICS OF THE DEFORMATION

The dynamics of accretionary prisms are controlled by the rheology of the prism material, basal shear stress, compressive stress on the back of the prism, and gravity (Dahlen *et al.* 1984). In the initial phase of prism growth, basal and compressive stresses dominate and the prism thickens, supported by shear stress on the megathrust at its base. Thrusts form perpendicular to the maximum compression direction (e.g. Davis *et al.* 1983), which in the Makran is approximately N–S, forming E–W trending folds and thrust faults (e.g. Harms *et al.* 1982). Once the gravitational potential energy due to the growth of topography reaches the maximum shear stress that can be supported on the megathrust, the topographic elevation can no longer increase and the range instead grows laterally by outwards migration of the thrust front (e.g. Molnar & Lyon-Caen 1988). The gravitational forces then balance the compressive stresses and the topography develops a wide, flat top, such as is seen in the Tibetan Plateau (e.g. Houseman & England 1986). Thrust structures which have been active during shortening and topographic growth may then become inactive, or be reactivated as strike-slip or normal faults.

In map view the shallow earthquakes in the Makran show clear spatial variations in the style of strain (Fig. 2a). Shallow thrust earthquakes (blue in Fig. 2a) occur offshore or near the coast, and most onshore earthquakes are strike-slip (red in Fig. 2a). Three strike-slip earthquakes, and an isolated thrust event, are the only examples of shallow (<15 km) seismic deformation in the central part of the onshore accretionary prism. The majority of the strike-slip earthquakes are concentrated at the lateral edges of the prism. This distribution of strain, and specifically the recent strike-slip earthquakes in the onshore Makran (e.g. Avouac *et al.* 2014; Penney *et al.* 2015), imply that the top of the Makran accretionary prism is no longer thickening. Additionally, the topography of the prism shows a flat top (see Fig. 3), indicating that a balance may have been reached between gravitational potential energy contrasts and the shear stresses on the megathrust. In this case, we can estimate the mean shear stress on the megathrust using the method of Lamb (2006). We will first discuss the deformation of the onshore part of the wedge and then the material properties of the megathrust.

5.1 Strike-slip faulting on the wedge top

The September 2013 M_w 7.7 Balochistan earthquake occurred on the Hoshab fault (Fig. 1; Fig. 9) at the eastern end of the Makran accretionary prism. The Hoshab fault is curved, and the sense of motion was left-lateral strike-slip along the entire 200 km rupture length (e.g. Avouac *et al.* 2014). This earthquake has been extensively studied (e.g. Avouac *et al.* 2014; Barnhart *et al.* 2014a; Jolivet *et al.* 2014), both because of its clear surface ruptures (e.g. Vallage *et al.* 2015) and its unusual geometry (e.g. Zhou *et al.* 2015). We do not address the complexities of the rupture dynamics here, but consider the earthquake's role in the regional deformation and its implications for the dynamics of the accretionary prism. Avouac *et al.* (2014) proposed that the southern part of the Makran accretionary prism is being extruded to the east, such that strike-slip motion on the Hoshab fault is kinematically favourable. However, GPS velocities south of the Hoshab fault do not show eastwards extrusion of the prism (Fig. 9b). The velocity field shows N–S compression of ∼10 mm yr^{-1} across the region of the fault (Fig. 9; Frohling & Szeliga 2016). Barnhart *et al.* (2014b) proposed 'ball-and-socket' rotations, whereby the regions north and south of the Hoshab fault rotate relative to each other about a pole in central Afghanistan. However, Barnhart *et al.* (2015) pointed out that such rotations cannot accommodate the shortening observed in the GPS, and appeal to alternating earthquake styles on the Hoshab fault, with a mixture of thrust and strike-slip events. From detailed comparison of the offsets resulting from the 2013 earthquake with other Quaternary offsets visible along the Hoshab fault, Zhou *et al.* (2015) found the Balochistan earthquake to be typical of Quaternary events on the Hoshab fault, making alternating earthquake styles unlikely. NE–SW left-lateral faulting, such as that observed in the Balochistan earthquake, can accommodate N–S compression if the fault-bounded blocks rotate about vertical axes (Fig. 9a; McKenzie & Jackson 1983; Campbell *et al.* 2013). Unlike the vertical-axis rotations described in Section 4.2, which accommodate simple shear of horizontal planes, the configuration shown in Fig. 9(a) accommodates pure shear. Using the geometry shown in Fig. D2, we find

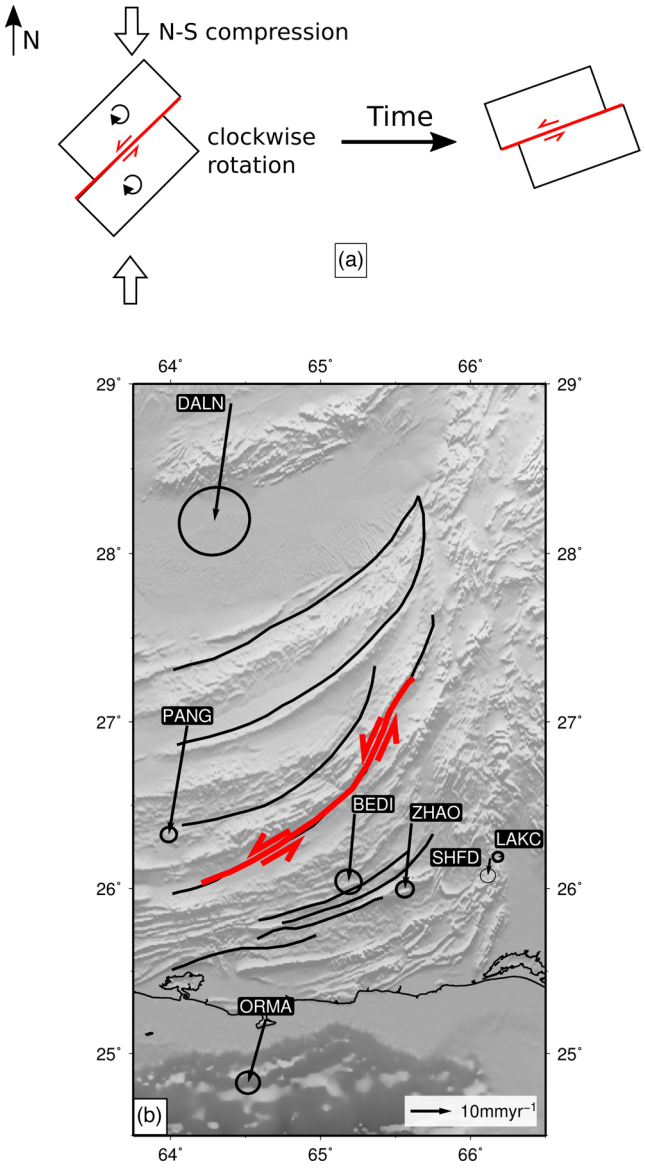

Figure 9. Kinematics of the Hoshab fault. (a) The Hoshab fault accommodates N–S compression (white arrows) by clockwise rotation and left-lateral faulting. (b) Fault map of the eastern Makran, after Lawrence *et al.* (1981). The trace of surface ruptures on the Hoshab fault from Avouac *et al.* (2014) is shown in red. Black arrows show GPS velocities relative to stable Arabia with 95 per cent confidence ellipses (Frohling & Szeliga 2016). The velocity difference between PANG, to the north, and BEDI and ZHAO, to the south, shows only shortening, with no eastwards extrusion of the southern part of the prism.

that a rotation rate of 2.4° Myr^{-1} would allow the Hoshab fault, and other nearby structures, to accommodate the regional shortening by strike-slip faulting, without requiring that the sense of slip changes between earthquakes. The E–W extension resulting from these rotations is very small, which is in better agreement with the almost purely N–S velocity field (Fig. 9b) than the extrusion model of Avouac *et al.* (2014). Our kinematic model is, therefore, consistent with both the GPS and the geometry of the Balochistan earthquake, in contrast to models proposed by earlier authors (Avouac *et al.* 2014; Barnhart *et al.* 2014b, 2015). There is, however, an outstanding question as to why shortening is not accommodated by thrusting, since the southern end of the Hoshab fault is optimally oriented to accommodate N–S compression by thrusting and topographic growth, as it strikes E–W and dips 50–70° (Avouac *et al.* 2014). The alternative kinematic style we observe, in which N–S compression is accommodated by strike-slip faulting and rotation, suggests that the Hoshab fault, and similar sub-parallel structures, acted as thrusts in the early period of prism growth, when compressive stresses dominated, and have been reactivated as strike-slip faults, now that the gravitational potential energy of the wedge has reached the maximum that can be supported by shear stresses on the megathrust.

The M_w 6.1 2013 Minab earthquake, which occurred in the western Makran, was a left-lateral strike-slip event on a fault aligned approximately perpendicular to the regional compression direction (Penney *et al.* 2015). A series of similar faults accommodate N–S right-lateral simple shear in the velocity field by rotating clockwise about vertical axes, and are thought to be reactivated thrust faults which have been steepened during prism growth. The adjacent faults of the MZP accommodate part of the shear by simple right-lateral motion on N–S planes. It is likely that this contrast in kinematic styles is due to reactivation of pre-existing E–W trending structures in the region of the Minab earthquake. This suggests that there has also been a change in strain regime through time in the western Makran, as well as in the eastern Makran.

Fault reactivation in a new strain regime, seen in both the Minab and Balochistan earthquakes, supports our conclusion that the gravitational potential energy of the wedge and the shear stresses on the megathrust are now in balance in the Makran prism, such that the wedge has reached a limiting upper elevation, and now grows by outwards migration of the thrust front.

5.2 Megathrust shear stress

The balance between gravitational potential energy contrasts and megathrust shear stresses in the Makran allows us to use the method of Lamb (2006) to calculate the mean shear stress required on the Makran megathrust to support the elevation contrast we observe between the bathymetric trench and the top of the prism. These calculations assume that the mean horizontal and vertical normal stresses within the prism are equal; equivalent to the balance between gravitational and far-field compressive forces discussed above. The geometry for our calculations is shown in Fig. 10(a). We will refer to the overriding plate material in this model as the subduction wedge, after Lamb (2006). The total force exerted on the wedge, per unit length along strike, depends on the density structure of this subduction wedge and its thickness. We assume a constant crustal density, ρ_c, of 2860 kg m^{-3} to a depth of 40 km (d in Fig. 10a), which Maggi *et al.* (2000) and Manaman *et al.* (2011) suggest as the Moho depth in the Makran. For greater depths we use a constant mantle density, ρ_m, of 3300 kg m^{-3}. Lamb (2006) suggests that the volcanic arc should be considered as the back of the subduction wedge, so we consider total wedge thicknesses, L, between 40 and 80 km, consistent with the range of subduction interface depths inferred in Section 2.3. The mean elevation contrast between the bathymetric slope break, which we use as a proxy for the surface projection of the megathrust, and the back of the subduction wedge is ∼5 km, which we take as 'h' in Fig. 10(a). We assume that the topographic contrast is covered by water with a density of 1000 kg m^{-3} (Fig. 10a).

As discussed in Sections 2.3 and 3, the mean dip of the Arabian slab is poorly constrained. Since the volcanic arc lies slightly north of the increase in dip of the subduction interface that we infer from

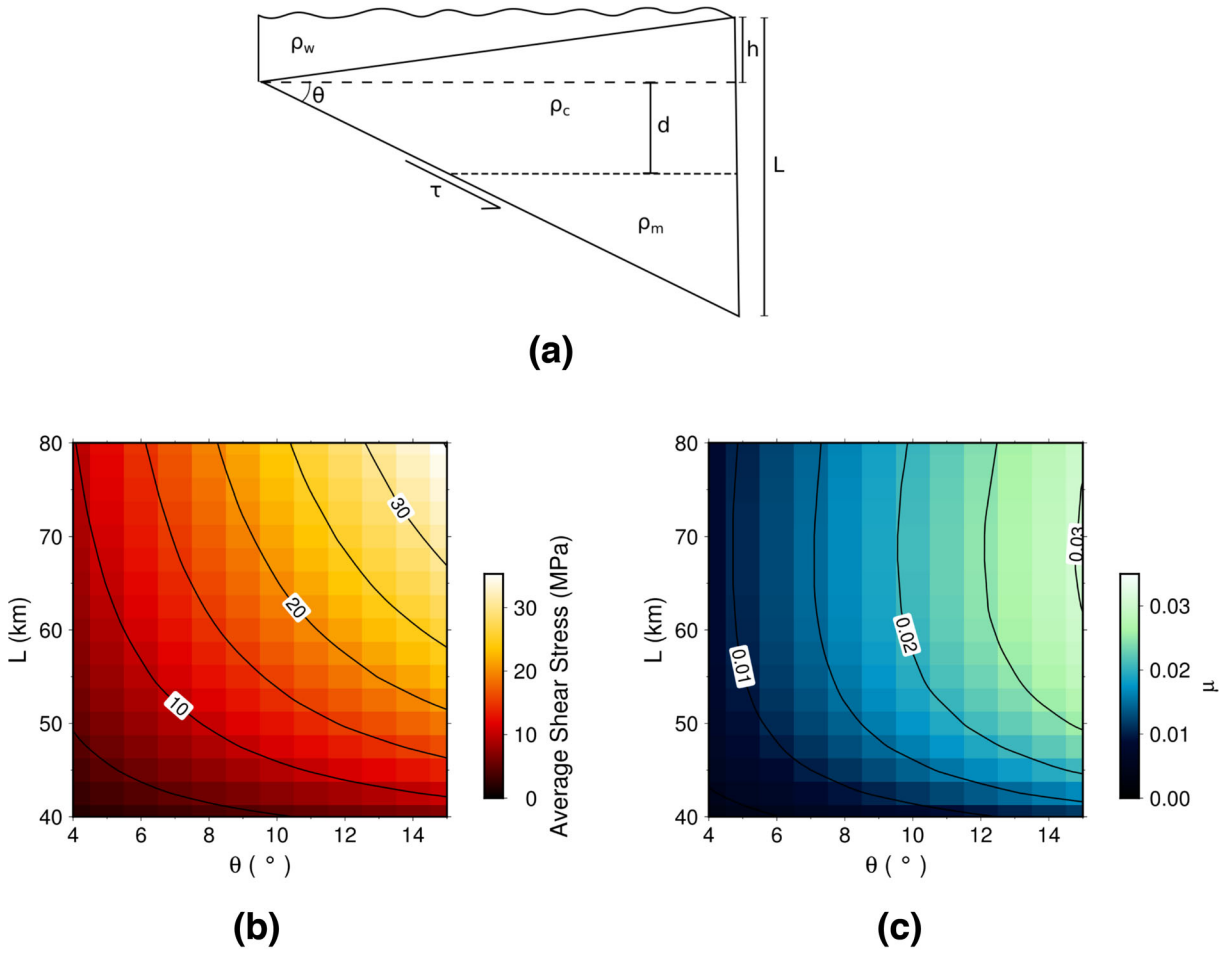

Figure 10. Megathrust rheology. (a) Geometry for calculating mean shear stress and coefficient of friction on the megathrust (after Lamb 2006). θ is the mean dip angle of the subduction interface. ρ_w, ρ_c and ρ_m are the water, crust and mantle densities respectively. d is the Moho depth. L is the depth of the back of the subduction wedge and h is the elevation contrast between the trench and the volcanic arc ($h \ll L$). τ is the mean shear stress on the megathrust. (b) Plot of the average shear stress required to support the topographic contrast above the subduction interface for different average dips, θ, and thicknesses of the subduction wedge, L. Contours are spaced at 5 MPa. (c) Plot of the effective coefficient of friction (mean shear stress divided by effective normal stress) required for different average dips, θ, and thicknesses of the subduction wedge, L. Contours are spaced at 0.005.

our earthquake profiles (Figs 2b and 3) we allow for steeper average dips than in our locking calculations, and use a range of dips from 4° to 15°. Figs 10(b) and (c) show the average shear stress and effective coefficient of friction (ratio of shear stress to normal stress) as a function of subduction wedge thickness, L, and mean dip angle, θ, calculated using the expressions of Lamb (2006). We estimate the mean shear stress on the interface to be between ∼5 and 35 MPa, and the effective coefficient of friction to be ∼0.01–0.03. These values of shear stress are consistent with those reported in other subduction zones (e.g. Von Herzen *et al.* 2001; Lamb 2006; Duarte *et al.* 2015). This suggests that neither the large sediment thickness of the Makran, which has been proposed to lubricate the plate interface through sediment underplating (e.g. Bayer *et al.* 2006), nor the low dip of the subduction interface, affect the mean shear stress on the megathrust.

6 CONCLUSIONS

A compilation of earthquakes with well-constrained depths and mechanisms allows us to place constraints on the position and shape of the subduction interface in the Makran subduction zone. GPS, geomorphology and structural analysis demonstrate that the N–S right-lateral shear across the SSZ is not accommodated either by thrusts or by rotating left-lateral faults at the zone's southern end. Instead, the motion may be transferred on to the right-lateral shear zone at the western end of the Makran accretionary prism. The megathrust in the western Makran may be locked and capable of producing large earthquakes, possibly with associated tsunamis. After such an earthquake we might expect normal-faulting earthquakes on the faults bounding the Jaz Murian depression.

There is strong evidence, from the Balochistan and Minab earthquakes, for a change from thrust to strike-slip faulting in the Makran accretionary prism at some point in the prism's history, suggesting that the gravitational potential energy of the prism has reached the maximum that can be supported by the shear stress on the megathrust. The mean shear stress (5–35 MPa) and effective coefficient of friction (0.01–0.03) are of similar magnitude to those in other subduction zones, despite the large sediment thicknesses on the subducting plate and the low dip angle of the subduction interface.

ACKNOWLEDGEMENTS

The authors would like to thank Rob Govers and Richard Walker for insightful reviews which improved the manuscript. This work

forms part of the NERC- and ESRC-funded project 'Earthquakes without Frontiers' and was partially supported by the NERC large grant 'Looking inside the Continents from Space'. CP is funded by an NERC studentship. Figures were prepared using the GMT package (Wessel *et al.* 2013). The facilities of IRIS Data Services, and specifically the IRIS Data Management Center, were used for access to waveforms, related metadata, and/or derived products used in this study. IRIS Data Services are funded through the Seismological Facilities for the Advancement of Geoscience and EarthScope (SAGE) Proposal of the National Science Foundation under Cooperative Agreement EAR-1261681.

REFERENCES

Acton, C.E., Priestley, K., Gaur, V.K. & Rai, S.S., 2010. Group velocity tomography of the Indo-Eurasian collision zone, *J. geophys. Res.,* **115**(12), 1–16.

Allen, M., Jackson, J. & Walker, R., 2004. Late Cenozoic reorganization of the Arabia-Eurasia collision and the comparison of short-term and long-term deformation rates, *Tectonics,* **23**(2), TC2008, doi:10.1029/2003TC001530.

Ambraseys, N.N. & Melville, C.P., 1982. *A History of Persian Earthquakes,* Cambridge Univ. Press.

Aron, F., Allmendinger, R.W., Cembrano, J., González, G. & Yáñez, G., 2013. Permanent fore-arc extension and seismic segmentation: Insights from the 2010 Maule earthquake, Chile, *J. geophys. Res.,* **118**(2), 724–739.

Arriagada, C. *et al.*, 2011. Nature and tectonic significance of co-seismic structures associated with the M_w 8.8 Maule earthquake, central-southern Chile forearc, *J. Struct. Geol.,* **33**(5), 891–897.

Asano, Y. *et al.*, 2011. Spatial distribution and focal mechanisms of aftershocks of the 2011 off the Pacific coast of Tohoku Earthquake, *Earth Planets Space,* **63**(7), 669–673.

Avouac, J.P., Tapponnier, P., Bai, M., You, H. & Wang, G., 1993. Active Thrusting and Folding Along the Northern Tien Shan and Late Cenozoic Rotation of the Tarim Relative to Dzungaria and Kazakhstan, *J. geophys. Res.,* **98**(B4), 6755–6804.

Avouac, J.-P. *et al.*, 2014. The 2013, M_w 7.7 Balochistan earthquake, energetic strike-slip reactivation of a thrust fault, *Earth Planet. Sci. Lett.,* **391,** 128–134.

Baker, C., 1993. The Active Seismicity and Tectonics of Iran, *PhD thesis,* University of Cambridge.

Baker, A., Allmendinger, R.W., Owen, L.A. & Rech, J.A., 2013. Permanent deformation caused by subduction earthquakes in northern Chile, *Nat. Geosci.,* **6**(6), 492–496.

Barnhart, W., Hayes, G., Briggs, R., Gold, R. & Bilham, R., 2014a. Ball-and-socket tectonic rotation during the 2013 M_w 7.7 Balochistan earthquake, *Earth Planet. Sci. Lett.,* **403,** 210–216.

Barnhart, W.D., Hayes, G.P., Samsonov, S.V., Fielding, E.J. & Seidman, L.E., 2014b. Breaking the oceanic lithosphere of a subducting slab: The 2013 Khash, Iran earthquake, *Geophys. Res. Lett.,* **41**(1), 32–36.

Barnhart, W., Briggs, R., Reitman, N., Gold, R. & Hayes, G., 2015. Evidence for slip partitioning and bimodal slip behavior on a single fault: Surface slip characteristics of the 2013 M_w 7.7 Balochistan, Pakistan earthquake, *Earth Planet. Sci. Lett.,* **420,** 1–11.

Bayasgalan, A., Jackson, J., Ritz, J. & Carretier, S., 1999a. Field examples of strike-slip fault terminations in Mongolia and their tectonic significance, *Tectonics,* **18**(3), 394–411.

Bayasgalan, A., Jackson, J., Ritz, J.F. & Carretier, S., 1999b. 'Forebergs', flower structures, and the development of large intracontinental strike-slip faults: The Gurvan Bogd fault system in Mongolia, *J. Struct. Geol.,* **21**(10), 1285–1302.

Bayer, R. *et al.*, 2006. Active deformation in Zagros-Makran transition zone inferred from GPS measurements, *Geophys. J. Int.,* **165**(1), 373–381.

Berberian, M., 1981. Active faulting and Tectonics of Iran, *Zagros, Hindu Kush Himalaya Geodynamic Evolution Series,* 3.

Berberian, M., Jackson, J., Qorashi, M., Khatib, M.M., Priestley, K., Talebian, M. & Ghafuri-Ashtiani, M., 1999. The 1997 May 10 Zirkuh (Qa'enat) earthquake (Mw 7.2): faulting along the Sistan suture zone of eastern Iran, *Geophys. J. Int.,* **136**(3), 671–694.

Berberian, M., Jackson, J., Qorashi, M., Talebian, M., Khatib, M. & Priestley, K., 2000. The 1994 Sefidabeh earthquakes in eastern Iran: blind thrusting and bedding-plane slip on a growing anticline, and active tectonics of the Sistan suture zone, *Geophys. J. Int.,* **142,** 283–299.

Berberian, M. *et al.*, 2001. The 1998 March 14 Fandoqa earthquake (Mw 6.6) in Kerman province, Southeast Iran: Re-rupture of the 1981 Sirch earthquake fault, triggering of slip on adjacent thrusts and the active tectonics of the Gowk fault zone, *Geophys. J. Int.,* **146**(2), 371–398.

Biabangard, H. & Moradian, A., 2008. Geology and geochemical evaluation of Taftan Volcano, Sistan and Baluchestan Province, southeast of Iran, *Chinese J. Geochemistry,* **27**(4), 356–369.

Bilham, R., Lodi, S. & Hough, S., 2007. Seismic hazard in Karachi, Pakistan: uncertain past, uncertain future, *Seismol. Res. Lett.,* **78**(6), 601–613.

Bouchon, M., Marsan, D., Durand, V., Campillo, M., Perfettini, H., Madariaga, R. & Gardonio, B., 2016. Potential slab deformation and plunge prior to the Tohoku, Iquique and Maule earthquakes, *Nat. Geosci.,* 9(May).

Bröcker, M., Fotoohi Rad, G., Burgess, R., Theunissen, S., Paderin, I., Rodionov, N. & Salimi, Z., 2013. New age constraints for the geodynamic evolution of the Sistan Suture Zone, eastern Iran, *Lithos,* **170–171**:17–34.

Byrne, D.E., Sykes, L.R. & Davis, D.M., 1992. Great thrust earthquakes and aseismic slip along the plate boundary of the Makran subduction zone, *J. geophys. Res.,* **97**(91), 449–478.

Campbell, G.E., Walker, R.T., Abdrakhmatov, K., Schwenninger, J., Jackson, J., Elliott, J.R. & Copley, A., 2013. The Dzhungarian fault: Late Quaternary tectonics and slip rate of a major right-lateral strike-slip fault in the northern Tien Shan region, *J. geophys. Res.,* **118**(10), 5681–5698.

Chandra, U., 1981. Focal mechanism solutions and their tectonic implications for the Eastern Alpine-Himalayan region, *Zagros, Hindu Kush, Himalaya Geodynamic Evolution Series,* **3,** 243–271.

Chandra, U., 1984. Focal mechanism solutions for earthquakes in Iran, *Phys. Earth planet. Inter.,* **34**(1), 9–16.

Chlieh, M., Avouac, J.P., Sieh, K., Natawidjaja, D.H. & Galetzka, J., 2008. Heterogeneous coupling of the Sumatran megathrust constrained by geodetic and paleogeodetic measurements, *J. geophys. Res.,* **113**(5), 1–31.

Conrad, G., Montigny, R., Thuizat, R. & Westphal, M., 1981. Tertiary and Quaternary geodynamics of southern Lut (Iran) as deduced from palaeomagnetic, isotopic and structural data, *Tectonophysics,* **75,** T11–T17.

Craig, T.J., Copley, A. & Jackson, J., 2014. A reassessment of outer-rise seismicity and its implications for the mechanics of oceanic lithosphere, *Geophys. J. Int.,* **197**(1), 63–89.

Dahlen, F.A., Suppe, J. & Davis, D., 1984. Mechanics of fold-and-thrust belts and accretionary wedges: Cohesive Coulomb theory, *J. geophys. Res.,* **89,** 10087–10101.

Davis, D., Suppe, J. & Dahlen, F.A., 1983. Mechanics of fold-and- thrust belts and accretionary wedges.*J. geophys. Res.,* **88**(B2), 1153–1172.

Dolati, A., 2010. Stratigraphy , structural geology and low-temperature thermochronology across the Makran accretionary wedge in Iran. *PhD thesis*, ETH Zurich.

Duarte, J.C., Schellart, W.P. & Cruden, A.R., 2015. How weak is the subduction zone interface? *Geophys. Res. Lett.,* **42**(8), 2664–2673.

Dugda, M.T., Nyblade, A.A. & Julia, J., 2007. Thin lithosphere beneath the Ethiopian Plateau revealed by a joint inversion of Rayleigh wave group velocities and receiver functions, *J. geophys. Res.,* **112**(8), 1–14.

Dykstra, J.D. & Birnie, R.W., 1979. Segmentation of the Quaternary Subduction Zone under the Baluchistan Region of Pakistan and Iran, in *Geodynamics of Pakistan,* pp. 319–323, eds Farah, A. & DeJong, K.A., Geological Survey of Pakistan.

Dziewonski, A.M., Chou, T. & Woodhouse, J.H., 1981. Determination of earthquake source parameters from waveform data for studies of global and regional seismicity, *J. geophys. Res.,* **86**(B4), 2825–2852.

Ebel, J.E., Bonjer, K.-P. & Oncescu, M., 2000. Paleoseismicity: seismicity evidence for past large earthquakes, *Seismol. Res. Lett.,* **71**(2), 283–294.

Ekström, G., Nettles, M. & Dziewoński, A.M., 2012. The global CMT project 2004-2010: centroid-moment tensors for 13,017 earthquakes, *Phys. Earth Planet. Inter.,* **200–201,** 1–9.

Ellouz-Zimmermann, N., Deville, E., Müller, C., Lallemant, S., Subhani, A. & Tabreez, A., 2007. Impact of sedimentation on convergent margin tectonics: example of the Makran accretionary prism (Pakistan), in *Thrust Belts and Foreland Basins,* chap. 17, pp. 327–350, eds Lacombe, O., Roure, F., Lavé, J. & Vergés, J., Springer, Berlin, Heidelberg.

England, P. & Wilkins, C., 2004. A simple analytical approximation to the temperature structure in subduction zones, *Geophys. J. Int.,* **159**(3), 1138–1154.

Engdahl, E.R., van der Hilst, R. & Buland, R., 1998. Global teleseismic earthquake relocation with improved travel times and procedures for depth determination, *Bull. seism. Soc. Am.,* **88**(3), 722–743.

England, P., Engdahl, R. & Thatcher, W., 2004. Systematic variation in the depths of slabs beneath arc volcanoes, *Geophys. J. Int.,* **156**(2), 377–408.

Engdahl, E.R., Jackson, J., Myers, S., Bergman, E. & Priestley, K., 2006. Relocation and assessment of seismicity in the Iran region, *Geophys. J. Int.,* **167**(2), 761–778.

Falcon, N., 1974. An outline of the geology of the Iranian Makran, *Geogr. J.,* **140**(2), 284–291.

Farías, M., Comte, D., Roecker, S., Carrizo, D. & Pardo, M., 2011. Crustal extensional faulting triggered by the 2010 Chilean earthquake: the Pichilemu seismic sequence, *Tectonics,* **30**(6), 1–11.

Freund, R., 1970. Rotation of strike slip faults in Sistan, southeast Iran, *J. Geol.,* **78**(2), 188–200.

Frohling, E. & Szeliga, W., 2016. GPS constraints on interplate locking within the Makran subduction zone, *Geophys. J. Int.,* **205**(1), 67–76.

Fruehn, J., White, R.S. & Minshull, T.A., 1997. Internal deformation and compaction of the Makran accretionary wedge, *Terra Nova,* **9**(3), 101–104.

Goldsworthy, M. & Jackson, J., 2001. Migration of activity within normal fault systems: examples from the quaternary of mainland Greece, *J. Struct. Geol.,* **23**(2–3), 489–506.

Haghipour, N. & Burg, J.-P., 2014. Geomorphological analysis of the drainage system on the growing Makran accretionary wedge, *Geomorphology,* **209,** 111–132.

Haghipour, N., Burg, J.-P., Kober, F., Zeilinger, G., Ivy-Ochs, S., Kubik, P.W. & Faridi, M., 2012. Rate of crustal shortening and non-Coulomb behaviour of an active accretionary wedge: the folded fluvial terraces in Makran (SE, Iran), *Earth Planet. Sci. Lett.,* **355–356,** 187–198.

Harms, J.C., Cappel, H.N. & Francis, D.C., 1982. *Geology and Petroleum Potential of the Makran Coast, Pakistan*, Society of Petroleum Engineers.

Harrison, J.V., 1943. The Jaz Murian depression, Persian Baluchistan, *Geogr. J.,* **101**(5/6), 206–225.

Heidarzadeh, M. & Kijko, A., 2011. A probabilistic tsunami hazard assessment for the Makran subduction zone at the northwestern Indian Ocean, *Nat. Hazards,* **56**(3), 577–593.

Herring, T., King, R. & McClusky, S., 2010. Documentation for the GAMIT/GLOBK GPS processing software release 10.4. *Technical report*, Mass. Inst. of Technol., Cambridge.

Hicks, S.P. & Rietbrock, A., 2015. Seismic slip on an upper-plate normal fault during a large subduction megathrust rupture, *Nat. Geosci.,* **8,** 955–960.

Hoffmann, G., Rupprechter, M., Balushi, N.A., Grützner, C. & Reicherter, K., 2013. The impact of the 1945 Makran tsunami along the coastlines of the Arabian Sea (Northern Indian Ocean) - a review, *Z. Geomorphol. Suppl. Issues,* **57**(4), 257–277.

Hoffmann, G., Grützner, C., Reicherter, K. & Preusser, F., 2015. Geoarchaeological evidence for a Holocene extreme flooding event within the Arabian Sea (Ras al Hadd, Oman), *Quat. Sci. Rev.,* **113,** 123–133.

Houseman, G. & England, P., 1986. Finite strain calculations of continental deformation. 1. Method and general results for convergence zones, *J. geophys. Res.,* **91**(B3), 3651–3663.

Hyndman, R., Yamano, M. & Oleskevich, D., 1997. The Seismogenic Zone of Subduction Thrust Faults, *Isl. Arc,* **6,** 244–260.

International Seismological Centre, 2015. *On-line Bulletin*, http://www.isc.ac.uk, Internatl. Seismol. Cent., Thatcham, United Kingdom.

Isacks, B.L. & Barazangi, M., 1977. Geometry of Benioff zones: Lateral segmentation and downwards bending of the subducted lithosphere, in *Island Arcs, Deep Sea Trenches and Back-Arc Basins,* pp. 99–114, eds Talwani, M. & Pitman, W.C., American Geophysical Union.

Jackson, J., 1980. Errors in focal depth determination and the depth of seismicity in Iran and Turkey, *Geophys. J. R. astr. Suc.,* **61,** 285–301.

Jackson, J. & McKenzie, D., 1984. Active tectonics of the Alpine-Himalayan belt between western Turkey and Pakistan, *Geophys. J. Int.,* **77,** 185–264.

Jackson, J., Priestley, K., Allen, M. & Berberian, M., 2002. Active tectonics of the South Caspian Basin, *Geophys. J. Int.,* **148**(2), 214–245.

Jackson, J. *et al.*, 2006. Seismotectonic, rupture process, and earthquake-hazard aspects of the 2003 December 26 Bam, Iran, earthquake, *Geophys. J. Int.,* **166**(3), 1270–1292.

Jacob, K.H. & Quittmeyer, R., 1979. The Makran region of Pakistan and Iran: trench-arc system with active plate subduction, in *Geodynamics of Pakistan,* pp. 305–318, eds Farah, A. & DeJong, K.A., Geological Survey of Pakistan.

Jolivet, R. *et al.*, 2014. The 2013 M_w 7.7 Balochistan earthquake: seismic potential of an accretionary wedge, *Bull. seism. Soc. Am.,* **104**(2), 1020–1030.

Julià, J., Ammon, C.J., Herrmann, R.B. & Correig, A.M., 2000. Joint inversion of receiver function and surface wave dispersion observations, *Geophys. J. Int.,* **143**(1), 99–112.

Julià, J., Ammon, C.J. & Herrmann, R.B., 2003. Lithospheric structure of the Arabian Shield from the joint inversion of receiver functions and surface-wave group velocities, *Tectonophysics,* **371**(1–4), 1–21.

Kennett, B. L.N., Engdahl, E.R. & Buland, R., 1995. Constraints on seismic velocities in the Earth from traveltimes, *Geophys. J. Int.,* **122,** 108–124.

Konca, O. *et al.*, 2008. Partial rupture of a locked patch of the Sumatra megathrust during the 2007 earthquake sequence, *Nature,* **456**(7222), 631–635.

Kopp, C., Fruehn, J., Flueh, E., Reichert, C., Kukowski, N., Bialas, J. & Klaeschen, D., 2000. Structure of the Makran subduction zone from wide-angle and reflection seismic data, *Tectonophysics,* **329,** 171–191.

Kukowski, N., Schillhorn, T., Flueh, E. & Huhn, K., 2000. Newly identified strike-slip plate boundary in the northeastern Arabian Sea, *Geology,* **123,** 355–358.

Laane, J.L. & Chen, W.-P., 1989. The Makran earthquake of 1983 April 18: A possible analogue to the Puget Sound earthquake of 1965?, *Geophys. J. Int.,* **98,** 1–9.

Lamb, S., 2006. Shear stresses on megathrusts: implications for mountain building behind subduction zones, *J. geophys. Res.,* **111**(B7), B07401, doi:10.1029/2005JB003916.

Langston, C.A., 1979. Structure under Mount Rainier, Washington, inferred from teleseismic body waves, *J. geophys. Res.,* **84**(B9), 4749–4762.

Lawrence, R.D., Yeats, R.S., Khan, S.H., Farah, A. & DeJong, K.A., 1981. Thrust and strike slip fault interaction along the Chaman transform zone, Pakistan, *Geol. Soc. London, Spec. Publ.,* **9**(1), 363–370.

Lay, T. *et al.*, 2005. The Great Sumatra-Andaman earthquake of 26 December 2004, *Science,* **308,** 1127–1133.

Ligorría, J.P. & Ammon, C.J., 1999. Iterative deconvolution and receiver-function estimation, *Bull. seism. Soc. Am.,* **89**(5), 1395–1400.

Lin, N.Y., Jolivet, R., Simons, M., Agram, P.S., Martens, H.R., Li, Z. & Lodi, S.H., 2015. High interseismic coupling in the Eastern Makran (Pakistan) subduction zone, *Earth Planet. Sci. Lett.,* **420,** 116–126.

Loveless, J.P., Allmendinger, R.W., Pritchard, M.E. & González, G., 2010. Normal and reverse faulting driven by the subduction zone earthquake cycle in the northern Chilean fore arc, *Tectonics,* **29**(2), 1–16.

Maggi, A., Jackson, J.A., Priestley, K. & Baker, C., 2000. A re-assessment of focal depth distributions in southern Iran, the Tien Shan and northern India: do earthquakes really occur in the continental mantle?, *Geophys. J. Int.,* **143**(3), 629–661.

Manaman, N.S., Shomali, H. & Koyi, H., 2011. New constraints on upper-mantle*S*-velocity structure and crustal thickness of the Iranian plateau using partitioned waveform inversion, *Geophys. J. Int.*, **184**(1), 247–267.

Masson, F., Anvari, M., Djamour, Y., Walpersdorf, A., Tavakoli, F., Daignières, M., Nankali, H. & Van Gorp, S., 2007. Large-scale velocity field and strain tensor in Iran inferred from GPS measurements: new insight for the present-day deformation pattern within NE Iran, *Geophys. J. Int.,* **170**(1), 436–440.

McCaffrey, R. & Abers, G., 1988. *SYN3: A program for inversion of teleseismic body waveforms on microcomputers*. *Technical report*, Air Force Geophysics Laboratory Technical Report.

McCaffrey, R., Abers, G. & Zwick, P., 1991. Inversion of teleseismic body waves, in *Digital Seismogram Analysis and Waveform Inversion,* pp. 81–166, ed. Lee, W., Int. Assoc. Seismol. Phys. Earth Inter. Software Library.

McKenzie, D. & Jackson, J., 2012. Tsunami earthquake generation by the release of gravitational potential energy, *Earth Planet. Sci. Lett.,* **345–348,** 1–8.

McKenzie, D. & Jackson, J., 1986. A block model of distributed deformation by faulting, *J. Geol. Soc. London,* **143,** 349–353.

McKenzie, D. & Jackson, J.A., 1983. The relationship between strain rates, crustal thickening, paleomagnetism, finite strain, and fault movement within a deforming zone, *Earth Planet. Sci. Lett.,* **65,** 182–202.

Meyer, B. & Le Dortz, K., 2007. Strike-slip kinematics in Central and Eastern Iran: estimating fault slip-rates averaged over the Holocene, *Tectonics,* **26,** TC5009, doi:10.1029/2006TC002073.

Molnar, P. & Lyon-Caen, H., 1988. Some simple physical aspects of the support, structure, and evolution of mountain belts, *GSA Spec. Pap.,* **218,** 179–208.

Molnar, P. & Lyon-Caen, H., 1989. Fault plane solutions of earthquakes and active tectonics of the Tibetan Plateau and its margins, *Geophys. J. Int.,* **99**(1), 123–154.

Morgan, K.H., McCall, G. J.H. & Huber, H., 1979. Minab Quadrangle, *Technical report*, Geological and Mineral Survey of Iran.

Musson, R. M.W., 2009. Subduction in the Western Makran: the historian's contribution, *J. Geol. Soc. London,* **166**(3), 387–391.

Natawidjaja, D.H., Sieh, K., Ward, S.N., Cheng, H., Edwards, R.L., Galetzka, J. & Suwargadi, B.W., 2004. Paleogeodetic records of seismic and aseismic subduction from central Sumatran microatolls, Indonesia, *J. geophys. Res,* **109**(4), 1–34.

Niazi, M., Shimamura, H. & Matsu'ura, M., 1980. Microearthquakes and crustal structure off the Makran coast of Iran, *Geophys. Res. Lett.,* **7**(5), 2–5.

Nicholson, K.N., Khan, M. & Mahmood, K., 2010. Geochemistry of the Chagai-Raskoh arc, Pakistan: complex arc dynamics spanning the Cretaceous to the Quaternary, *Lithos,* **118**(3–4), 338–348.

Nissen, E., Yamini-Fard, F., Tatar, M., Gholamzadeh, A., Bergman, E., Elliott, J., Jackson, J. & Parsons, B., 2010. The vertical separation of mainshock rupture and microseismicity at Qeshm island in the Zagros fold-and-thrust belt, Iran, *Earth Planet. Sci. Lett.,* **296**(3–4), 181–194.

Nissen, E., Tatar, M., Jackson, J. & Allen, M., 2011. New views on earthquake faulting in the Zagros fold-and-thrust belt of Iran, *Geophys. J. Int.,* **186**(3), 928–944.

Nur, A., Ron, H. & Scotti, O., 1986. Fault mechanics and the kinematics of block rotations, *Geology,* **14**(9), 746–749.

Okada, Y., 1985. Surface deformation due to shear and tensile faults in a half-space, *Bull. seism. Soc. Am.,* **75**(4), 1135–1154.

Page, W.D., Alt, J.N., Cluff, L.S. & Plafker, G., 1979. Evidence for the recurrence of large-magnitude earthquakes along the Makran coast of Iran and Pakistan, *Tectonophysics,* **52**(1–4), 533–547.

Penney, C., Copley, A. & Oveisi, B., 2015. Subduction tractions and vertical axis rotations in the Zagros-Makran transition zone, SE Iran: the 2013 May 11 Mw 6.1 Minab earthquake, *Geophys. J. Int.,* **202**(2), 1122–1136.

Peyret, M. *et al.*, 2009. Present-day strain distribution across the Minab-Zendan-Palami fault system from dense GPS transects, *Geophys. J. Int.,* **179**(2), 751–762.

Platt, J.P., Leggett, J.K., Young, J., Raza, H. & Alam, S., 1985. Large-scale sediment underplating in the Makran accretionary prism, southwest Pakistan.*Geology,* **13**(7), 507–511.

Priestley, K., James, J. & Mckenzie, D., 2008. Lithospheric structure and deep earthquakes beneath India, the Himalaya and southern Tibet, *Geophys. J. Int.,* **172**(1), 345–362.

Regard, V. *et al.*, 2005. Cumulative right-lateral fault slip rate across the Zagros-Makran transfer zone: role of the Minab-Zendan fault system in accommodating Arabia-Eurasia convergence in southeast Iran, *Geophys. J. Int.,* **162**(1), 177–203.

Reilinger, R. *et al.*, 2006. GPS constraints on continental deformation in the Africa-Arabia-Eurasia continental collision zone and implications for the dynamics of plate interactions, *J. geophys. Res.,* **111**(B5), B05411, doi:10.1029/2005JB004051.

Saadat, S. & Stern, C.R., 2011. Petrochemistry and genesis of olivine basalts from small monogenetic parasitic cones of Bazman stratovolcano, Makran arc, southeastern Iran, *Lithos,* **125**(1-2), 607–619.

Savage, J.C., 1983. A dislocation model of strain accumulation and release at a subduction zone, *J. geophys. Res.,* **88,** 4984–4996.

Scott, C.P., Allmendinger, R.W., González, G. & Loveless, J.P., 2016. Coseismic extension from surface cracks reopened by the 2014 Pisagua, northern Chile, earthquake sequence, *Geology,* **44**(5), 387–390.

Smith, G., McNeill, L., Henstock, T.J. & Bull, J., 2012. The structure and fault activity of the Makran accretionary prism, *J. geophys. Res.,* **117,** B07407, doi:10.1029/2012JB009312.

Smith, G.L., McNeill, L.C., Wang, K., He, J. & Henstock, T.J., 2013. Thermal structure and megathrust seismogenic potential of the Makran subduction zone, *Geophys. Res. Lett.,* **40**(8), 1528–1533.

Syracuse, E.M. & Abers, G.A., 2006. Global compilation of variations in slab depth beneath arc volcanoes and implications, *Geochem. Geophys. Geosyst.,* **7,** Q05017, doi:10.1029/2005GC001045.

Talebian, M. *et al.*, 2006. The Dahuiyeh (Zarand) earthquake of 2005 February 22 in central Iran: reactivation of an intramountain reverse fault, *Geophys. J. Int.,* **164**(1), 137–148.

Taymaz, T., 1990. Earthquake mechanisms in the Hellenic Trench near Crete, *Geophys. J. Int.,* **102,** 695–731.

Tichelaar, B.W. & Ruff, L.J., 1993. Depth of seismic coupling along subduction zones, *J. geophys. Res.,* **98**(B2), 2017–2037.

Tirrul, R., Bell, I.R., Griffis, R.J. & Camp, V.E., 1983. The Sistan suture zone of eastern Iran, *Geol. Soc. Am. Bull.,* **94**(1), 134–150.

Tirrul, R., Griffis, R.J. & Camp, V.E., 1980. *Geology of the Zabol Quadrangle, 1.250,000*: Report submitted to the Geological and Mineral Survey of Iran.

Vallage, A., Klinger, Y., Grandin, R., Bhat, H.S. & Pierrot-Deseilligny, M., 2015. Inelastic surface deformation during the 2013 M_w 7.7 Balochistan, Pakistan, earthquake, *Geology,* **43**(12), 1079–1082.

Vernant, P. *et al.*, 2004. Present-day crustal deformation and plate kinematics in the Middle East constrained by GPS measurements in Iran and northern Oman, *Geophys. J. Int.,* **157**(1), 381–398.

Von Herzen, R., Ruppel, C., Molnar, P., Nettles, M., Nagihara, S. & Ekström, G., 2001. A constraint on the shear stress at the Pacific-Australian plate boundary from heat flow and seismicity at the Kermadec forearc, *J. geophys. Res.,* **106**(B4), 6817–6833.

Walker, R.T., 2003. Active faulting and tectonics of Eastern Iran, *PhD thesis,* University of Cambridge.

Walker, R. & Jackson, J., 2004. Active tectonics and late Cenozoic strain distribution in central and eastern Iran, *Tectonics,* **23**(5), TC5010, doi:10.1029/2003TC001529.

Walker, R., Jackson, J. & Baker, C., 2003. Surface expression of thrust faulting in eastern Iran: source parameters and surface deformation of the 1978 Tabas and 1968 Ferdows earthquake sequences, *Geophys. J. Int.,* **152**(3), 749–765.

Walker, R., Jackson, J. & Baker, C., 2004. Active faulting and seismicity of the Dasht-e-Bayaz region, eastern Iran, *Geophys. J. Int.,* **157**(1), 265–282.

Walker, R.T., Talebian, M., Sloan, R.A., Rasheedi, A., Fattahi, M. & Bryant, C., 2010. Holocene slip-rate on the Gowk strike-slip fault and implications for the distribution of tectonic strain in eastern Iran, *Geophys. J. Int.,* **181**(1), 221–228.

Walker, R.T. *et al.*, 2013. The 2010–2011 South Rigan (Baluchestan) earthquake sequence and its implications for distributed deformation and earthquake hazard in southeast Iran, *Geophys. J. Int.,* **193**(1), 349–374.

Walpersdorf, A. *et al.*, 2006. Difference in the GPS deformation pattern of North and Central Zagros (Iran), *Geophys. J. Int.,* **167**(3), 1077–1088.

Walpersdorf, A. *et al.*, 2014. Present-day kinematics and fault slip rates in eastern Iran, derived from 11 years of GPS data, *J. geophys. Res.,* **119,** 1359–1383.

Wessel, P., Smith, W. H.F., Scharroo, R., Luis, J. & Wobbe, F., 2013. Generic mapping tools: improved version released, *EOS, Trans. Am. geophys. Un.,* **94**(45), 409–410.

White, R. & Klitgord, K., 1976. Sediment deformation and plate tectonics in the Gulf of Oman, *Earth Planet. Sci. Lett.,* **32,** 199–209.

White, R.S. & Louden, K.E., 1982. The Makran continental margin: structure of a thickly sedimented convergent plate boundary, in *Studies in Continental Margin Geology,* vol. 34, pp. 499–518, eds Watkins, J.S. & Drake, C.L., American Association of Petroleum Geologists.

Ye, L., Lay, T., Kanamori, H. & Rivera, L., 2016. Rupture characteristics of major and great (Mw $\geq$ 7.0) megathrust earthquakes from 1990 to 2015: II. Depth dependence, *J. geophys. Res.,* **121,** 845–863.

Zhou, Y., Elliott, J.R., Parsons, B. & Walker, R.T., 2015. The 2013 Balochistan earthquake: an extraordinary or completely ordinary event?, *Geophys. Res. Lett.,* **42**(15), 6236–6243.

Zwick, P., McCaffrey, R. & Abers, G., 1994. *MT5 program*, in IASPEI Software Library, number 4, IASPEI.

APPENDIX A: EARTHQUAKE COMPILATION

Table A1 gives the source parameters of the well-constrained earthquakes plotted in Figs 2(b) and 3, and references where relevant. 1: Byrne *et al.* (1992); 2: Jackson & McKenzie (1984); 3: Jacob & Quittmeyer (1979); 4: Baker (1993); 5: Maggi *et al.* (2000) († indicates that only the earthquake depth has been waveform modelled, with the mechanism from the CMT); 6: Berberian *et al.* (2001); 7: Laane & Chen (1989); 8: Berberian *et al.* (2000); 9: Walker (2003), 10: Nissen *et al.* (2011); 11: Jackson *et al.* (2006); 12: Talebian *et al.* (2006); 13: Nissen *et al.* (2010); 14: Barnhart *et al.* (2014b); 15: Penney *et al.* (2015); 16: Jolivet *et al.* (2014); *: this study.

APPENDIX B: BODY-WAVEFORM MODELLING

This appendix shows our minimum misfit earthquake solutions from body-waveform modelling. We use Zwick *et al.*'s (1994) MT5 implementation of the method proposed by McCaffrey & Abers (1988) and McCaffrey *et al.* (1991). We use teleseismic (30°–90° epicentral distance) *P* and *SH* arrivals at GDSN stations downloaded from the IRIS DMC. These are deconvolved from their original instrument response and reconvolved with a WWSSN Long Period (15–100) response. Earthquakes are modelled as double-couple point sources and we invert direct waves and their associated depth phases for centroid depth, source geometry (strike, dip and rake), seismic moment and source–time function. The arrivals are manually picked from the broad-band seismogram where possible. The details of this technique have been described extensively elsewhere (e.g. Taymaz 1990; Maggi *et al.* 2000) so will not be repeated here. A realistic velocity model for this region is likely to be highly complex but, since the velocity structure is not well-constrained, we adopt a simplified velocity model. For the 2017 February 17 event we use a single layer velocity model with Vp 6.5 km s^{-1}, Vs 3.7 km s^{-1} and density 2800 kg m^{-3}. Four of the earthquakes for which we present solutions had catalogue depths significantly deeper than 40 km, which is the Moho depth reported in this region (Maggi *et al.* 2000; Manaman *et al.* 2011). For these events we use a two-layer velocity model; a 40 km upper layer with Vp 6.5 km s^{-1}, Vs 3.75 km s^{-1} and density 2860 kg m^{-3} and a half-space with Vp 7.8 km s^{-1}, Vs 4.5 km s^{-1} and density 3300 kg m^{-3}. The other two events have EHB depths of ~40 km, making the choice of velocity model problematic. We try the two-layer velocity model described above in both cases but find that a simpler single layer model with Vp 6.5 km s^{-1}, Vs 3.7 km s^{-1} and density 2800 kg m^{-3} is sufficient to provide a good fit to the data.

APPENDIX C: RECEIVER FUNCTIONS

We use seismograms from broad-band seismometers at Chabahar and Turbat (CHBR and TURB in Fig. 1) to determine receiver functions and combine these with surface waves to find the velocity structure beneath these sites (Section 2.3, Figs 3a and b). This method has been used extensively by other authors (e.g. Julià *et al.* 2003; Dugda *et al.* 2007; Priestley *et al.* 2008) and is described in detailed in Julià *et al.* (2000). Radial receiver functions are waveforms created by deconvolving the vertical component of the seismogram from the radial component to isolate the effect of the velocity structure at the receiver site from the other information in the teleseismic *P*-wave coda. The resulting radial-component time series corresponds closely to the impulse response of the Earth structure beneath the seismograph site (Langston 1979). Teleseismic receiver functions from earthquakes in the 30°–90° distance range recorded at these sites were determined using the iterative deconvolution method of Ligorría & Ammon (1999) and stacked in narrow backazimuth bins. The receiver functions from both sites show a strong, positive conversion, marked Ps in Fig. C1, at about 4 s which probably corresponds to the top of the subducting Arabian slab.

P-wave receiver functions are sensitive to the shear wave velocity (Vs). The delay time between the direct P arrival and the Ps conversion in the receiver function depends on the depth to the interface and the average wave speed of the overlying layer, creating a trade-off which means that neither the layer thickness nor the average wave speed of the layer can be uniquely determined through using only receiver-function analysis. To minimize this trade-off, we simultaneously model the *P*-wave receiver functions and 10–70 s period fundamental-mode Rayleigh-wave group velocities. We interpolated the group velocity maps of Acton *et al.* (2010) to obtain a site-specific dispersion curve. By modelling both data sets simultaneously we can place strong constraints on the velocity structure because the surface-wave dispersion is sensitive to the absolute velocity but less so to the layer thickness, whereas the receiver functions are sensitive to discontinuities in velocity but less so to absolute wave speed Julià *et al.* (2000). The dispersion constrains the average layer wave speed and thickness over a broader region around the site, and the receiver functions superimpose short wavelength details.

The starting Earth model in the receiver function-surface wave inversion is based on AK135 (Kennett *et al.* 1995) and parametrized as a stack of 2 km thick layers, except near the surface where 1 km-thick layers provide additional freedom in the inversion to fit any strong near-surface gradients. To minimize bias in the inversion result from an *a priori* choice of interface depth, we replaced the AK135 crustal wave speeds with the AK135 uppermost-mantle wave speeds so there is no *a priori* crustal structure in the starting inversion model. Perturbing the wave speed structure in the starting model by ±0.2 km s^{-1} has a negligible effect on the inverted structure. By making forward tests on the interface depth and we find that the depth of the sediment-basement interface is constrained to ±2 km.

Table A1. Source parameters of well-constrained earthquakes.

Date	Time	Lat	Lon	Depth (km)	M_w	Strike	Dip	Rake	Method	Ref
1945/11/27	21:57	25.15	63.48	27	8.1	246	7	89	BWM	1
1947/08/05	14:24	25.04	63.49	20	6.8	236	7	68	BWM	1
1962/09/01	15:51	25.60	65.22	18	5.3	251	10	80	FM	1
1964/12/22	04:37	28.2	57.00	18	6.1	92	76	90	FM	2
1966/10/29	08:59	27.631	65.572	47	–	–	–	–	d	–
1968/08/02	13:30	27.54	60.92	67	5.7	265	70	−80	FM	3
1968/08/03	14:02	25.19	62.87	26	4.7	290	49	−50	FM	1
1968/04/23	12:39	27.736	56.744	21	–	–	–	–	d	–
1969/02/13	11:11	24.99	62.75	28	5.1	279	9	84	FM	1
1969/11/07	18:34	27.80	60.02	74	6.5	279	82	−65	FM	3
1970/11/09	17:41	29.50	56.78	100	5.4	68	19	−124	BWM	4
1970/02/28	19:58	27.811	56.309	12	–	–	–	–	d	–
1970/04/01	23:54	27.918	56.687	28	–	–	–	–	d	–
1971/12/09	01:42	27.297	56.373	9	–	–	–	–	d	–
1972/08/08	19:10	25.14	61.22	18	5.0	95	82	77	BWM	1
1972/08/06	01:13	25.04	61.22	20	5.4	321	17	134	FM	1
1972/08/18	10:03	24.83	63.14	20	4.6	277	9	84	FM	1
1972/11/17	09:09	27.35	59.09	65	5.4	66	70	171	FM	2
1972/06/30	17:49	27.176	56.925	27	–	–	–	–	d	–
1972/08/02	21:33	27.953	56.814	21	–	–	–	–	d	–
1973/09/02	07:23	24.88	63.21	27	5.2	281	23	70	FM	1
1973/04/26	14:30	27.168	60.800	57	–	–	–	–	d	–
1973/08/25	14:58	28.111	56.762	17	–	–	–	–	d	–
1975/07/29	13:25	25.22	63.09	24	5.0	278	27	88	FM	1
1975/03/07	14:26	27.486	56.237	15	–	–	–	–	d	–
1977/03/22	11:57	27.60	56.42	12	6.0	77	34	112	BWM	5
1977/12/10	05:46	27.68	56.60	18	5.6	59	72	68	BWM	5
1977/12/19	23:34	30.851	56.508	7	5.9	231	69	4	ENG	–
1977/03/24	00:13	27.590	56.480	14	–	–	–	–	d	–
1977/04/30	14:35	27.562	56.499	13	–	–	–	–	d	–
1977/06/26	02:25	27.469	56.135	7	–	–	–	–	d	–
1977/06/28	03:44	27.514	56.158	6	–	–	–	–	d	–
1977/09/13	00:16	27.634	56.440	14	–	–	–	–	d	–
1978/02/10	20:51	25.33	62.40	24	5.1	106	85	105	FM	1
1978/03/16	02:01	29.93	66.30	10	5.9	193	89.9	−0.01	FM	2
1978/05/06	11:16	29.84	66.21	15	5.7	193	89.9	−0.01	FM	2
1978/02/22	20:17	28.116	56.885	20	–	–	–	–	d	–
1978/02/23	23:24	28.152	56.846	20	–	–	–	–	d	–
1979/01/10	01:26	26.55	60.95	3	5.8	256	61	13	BWM	1
1979/01/10	15:05	26.48	61.02	2	5.9	230	82	−4	BWM	1
1980/04/28	07:04	27.55	64.48	54	5.5	249	75	−82	BWM	5†
1980/04/28	07:05	27.54	64.50	60	5.3	259	87	−70	FM	1
1980/11/28	21:15	27.616	56.534	8	5.4	311	37	134	ENG	–
1980/09/06	21:29	28.505	65.962	9	–	–	–	–	d	–
1981/06/11	7:24	29.86	57.68	20	6.58	169	52	156	BWM	6
1981/07/28	17:22	29.99	57.79	18	6.98	177	69	−176	BWM	6
1981/04/16	10:27	27.715	56.353	29	5.1	125	85	132	ENG	–
1981/06/21	13:08	29.810	57.792	17	–	–	–	–	d	–
1981/07/28	19:05	30.107	57.598	10	–	–	–	–	d	–
1981/07/28	21:54	29.959	57.691	13	–	–	–	–	d	–
1981/10/14	09:12	29.805	57.689	11	–	–	–	–	d	–
1982/02/25	20:13	29.841	57.811	23	–	–	–	–	d	–
1982/07/11	13:19	27.843	56.278	13	–	–	–	–	d	–
1983/04/18	10:58	27.76	62.08	65	6.65	83	32	−67	BWM	7
1983/07/12	11:34	27.61	56.41	17	5.93	227	50	75	BWM	5
1983/02/07	15:06	26.866	57.570	21	6.0	5	42	172	ENG	–
1984/08/06	11:14	30.85	57.19	11	5.29	94	35	86	BWM	4
1984/01/18	14:08	28.005	65.765	8	5.6	349	50	−13	ENG	–
1984/10/02	03:19	26.922	66.253	3	5.3	191	76	0	ENG	–
1984/04/22	13:39	27.628	56.645	23	–	–	–	–	d	–
1984/10/11	05:09	29.476	57.962	14	–	–	–	–	d	–
1985/03/03	13:54	31.805	56.159	7	–	–	–	–	d	–
1985/06/22	12:41	29.450	61.152	13	–	–	–	–	d	–
1986/12/31	16:56	25.259	63.251	24	–	–	–	–	d	–
1987/04/19	05:53	28.00	56.87	19	5.5	219	47	13	BWM	5

Table 1. (*Continued*.)

Date	Time	Lat	Lon	Depth (km)	M_w	Strike	Dip	Rake	Method	Ref
1987/08/10	10:52	29.88	63.88	155	5.9	346	31	−50	BWM	5
1987/04/11	23:50	31.609	56.079	7	–	–	–	–	d	–
1987/05/26	19:23	31.595	60.176	16	–	–	–	–	d	–
1988/03/14	02:26	24.977	62.923	23	–	–	–	–	d	–
1989/11/20	04:19	29.90	57.72	10	5.83	145	69	−172	BWM	6
1989/12/07	12:59	25.915	58.970	11	5.9	142	37	103	ENG	–
1990/07/26	06:53	27.35	65.58	8	5.7	216	76	44	BWM	5
1990/09/26	15:32	29.14	60.91	8	5.5	15	76	166	BWM	4
1990/03/04	19:46	28.905	66.361	4	6.1	278	78	−176	ENG	–
1990/03/15	00:12	31.674	60.165	15	5.2	100	82	−1	ENG	–
1990/06/17	17:17	27.402	65.621	14	5.5	115	56	173	ENG	–
1990/08/14	00:50	27.043	66.046	15	5.5	287	71	−170	ENG	–
1990/06/26	04:59	28.433	59.094	12	–	–	–	–	d	–
1991/12/07	14:22	25.153	62.971	29	5.6	309	8	133	ENG	–
1991/08/08	11:12	26.878	65.911	46	–	–	–	–	d	–
1992/12/17	10:39	25.90	61.45	40	5.8	2	46	129	BWM	*
1992/01/20	08:58	27.549	66.118	18	5.5	99	72	170	ENG	–
1992/01/30	05:22	24.947	63.160	27	5.9	298	10	126	ENG	–
1992/02/05	23:10	31.391	66.840	15	5.5	299	87	−177	ENG	–
1992/08/28	00:50	29.193	66.808	7	5.6	118	67	179	ENG	–
1992/09/11	18:24	30.006	60.738	19	5.2	91	25	51	ENG	–
1992/03/09	16:59	27.503	66.197	17	–	–	–	–	d	–
1992/09/11	17:04	29.995	60.705	14	–	–	–	–	d	–
1993/04/12	14:00	28.269	57.130	29	5.0	292	44	97	ENG	–
1993/02/04	19:41	24.845	62.846	26	–	–	–	–	d	–
1993/12/19	11:45	25.245	62.573	25	–	–	–	–	d	–
1994/02/23	08:02	30.80	60.57	7	6.05	143	29	96	BWM	8
1994/02/24	00:11	30.82	60.53	10	6.20	155	45	110	BWM	8
1994/02/26	02:31	30.78	60.55	5	5.95	146	36	107	BWM	8
1994/02/28	11:13	30.82	60.55	6	5.49	122	33	78	BWM	8
1994/12/10	12:16	27.90	64.94	72	5.1	204	37	−130	BWM	5†
1994/02/23	11:54	30.830	60.514	9	5.5	108	31	62	ENG	–
1996/03/04	01:35	27.523	56.236	14	–	–	–	–	d	–
1996/04/10	21:50	28.080	56.773	21	–	–	–	–	d	–
1997/10/20	06:09	28.45	57.25	28	5.2	244	19	47	BWM	5
1997/07/27	23:33	27.419	56.621	22	5.1	108	76	175	ENG	–
1997/01/24	17:12	28.168	57.533	39	–	–	–	–	d	–
1997/02/17	04:31	27.376	56.141	17	–	–	–	–	d	–
1997/04/19	22:31	27.860	56.800	21	–	–	–	–	d	–
1997/09/08	06:31	24.218	63.260	27	–	–	–	–	d	–
1997/10/06	16:09	28.428	57.209	29	–	–	–	–	d	–
1998/03/14	19:40	30.08	57.61	5	6.57	156	54	−165	BWM	6
1998/06/10	8:30	28.22	58.49	85	5.25	235	87	−96	BWM	5
1998/01/05	16:58	28.947	64.364	15	5.1	48	37	104	ENG	–
1998/04/19	19:57	25.007	63.275	25	–	–	–	–	d	–
1998/05/28	20:32	26.551	62.167	36	–	–	–	–	d	–
1999/03/04	05:38	28.34	57.19	28	6.2	314	18	128	BWM	9
1999/01/14	22:12	28.951	56.288	25	5.0	210	44	−57	ENG	–
2001/05/26	23:14	31.670	63.742	17	–	–	–	–	d	–
2001/08/04	14:07	24.985	61.460	28	–	–	–	–	d	–
2001/08/12	11:03	27.519	57.691	19	–	–	–	–	d	–
2001/08/14	21:19	29.939	65.141	27	–	–	–	–	d	–
2001/11/22	17:00	27.731	57.476	25	–	–	–	–	d	–
2002/03/11	20:06	25.191	56.087	27	5.0	224	32	−103	ENG	–
2002/06/03	20:17	25.499	63.501	30	–	–	–	–	d	–
2003/01/14	14:14	27.97	62.33	56	5.4	82	43	−86	BWM	*
2003/02/14	10:29	27.96	56.78	23	5.2	312	25	115	BWM	10
2003/12/26	01:57	28.90	58.28	6	6.6	354	86	−178	BWM	11
2003/12/26	01:57	28.90	58.28	7	6.1	180	64	150	BWM	11
2003/06/24	06:52	27.301	61.010	60	5.5	97	45	−65	ENG	–
2003/07/06	16:04	27.953	57.710	24	5.0	102	48	7	ENG	–
2003/11/05	07:58	27.416	56.114	17	4.9	70	39	105	ENG	–
2003/03/25	01:33	27.704	65.165	50	–	–	–	–	d	–
2004/01/28	09:06	26.881	57.460	26	5.2	92	40	24	ENG	–
2005/02/22	02:25	30.77	56.74	7	6.4	270	60	104	BWM	12

Table 1. (*Continued*.)

Date	Time	Lat	Lon	Depth (km)	M_w	Strike	Dip	Rake	Method	Ref
2005/03/13	03:31	27.08	61.86	51	5.8	255	36	−85	BWM	*
2006/07/18	23:27	26.24	61.14	40	5.1	107	70	−3	BWM	*
2006/02/28	07:31	28.13	56.82	15	5.9	302	12	113	BWM	10
2006/08/31	02:28	30.267	57.545	19	–	–	–	–	d	–
2006/09/09	12:22	25.019	62.112	28	–	–	–	–	d	–
2008/09/17	17:43	26.96	56.10	6	5.1	269	56	88	BWM	13
2009/10/25	17:48	29.54	63.90	120	5.6	236	89	−89	BWM	*
2009/02/02	08:36	27.180	66.453	15	5.2	189	81	−6	ISC	–
2009/11/03	23:26	27.261	56.195	23	5.1	246	30	63	ISC	–
2010/12/20	18:42	28.33	59.19	5	6.5	213	85	173	BWM	9
2010/06/05	16:59	28.076	66.095	16	5.1	196	83	6	ISC	–
2010/07/31	06:52	29.582	56.748	15	5.5	211	60	−25	ISC	–
2010/08/14	20:18	28.244	66.394	27	5.2	208	83	−5	ISC	–
2011/01/18	20:23	28.70	63.98	69	7.1	216	70	−112	BWM	*
2011/01/27	08:39	28.17	59.04	9	6.2	221	87	176	BWM	9
2011/01/27	07:02	28.174	58.940	22	5.0	122	64	−29	ISC	–
2011/01/28	04:20	28.129	59.040	26	5.3	133	74	−14	ISC	–
2011/03/05	20:42	28.281	57.130	28	5.2	93	87	86	ISC	–
2011/06/15	01:05	27.950	57.657	33	5.5	333	45	157	ISC	–
2011/06/26	19:46	30.035	57.653	25	5.2	114	36	71	ISC	–
2011/07/24	10:38	28.218	66.417	32	5.0	213	64	8	ISC	–
2011/08/10	00:53	27.767	65.136	44	5.9	11	72	−163	ISC	–
2012/02/27	18:48	31.401	56.778	24	5.3	89	40	59	ISC	–
2012/04/18	17:40	27.861	58.106	71	5.2	76	54	−164	ISC	–
2013/04/16	10:44	28.11	62.05	60	7.7	233	59	−109	BWM	14
2013/05/11	02:08	26.55	57.73	6	6.4	259	89	5	BWM	15
2013/05/12	00:07	26.39	57.52	8	5.5	86	88	10	BWM	15
2013/05/12	10:54	26.71	57.77	9	5.4	85	85	5	BWM	15
2013/09/24	11:30	26.50	65.50	15	7.7	230	47	8	BWM	16
2013/09/28	07:34	27.10	65.50	15	6.7	200	70	26	BWM	16
2013/01/21	19:48	30.356	57.518	15	5.4	235	70	13	ISC	–
2017/02/07	22:03	25.22	63.27	29	6.3	288	8	105	BWM	*

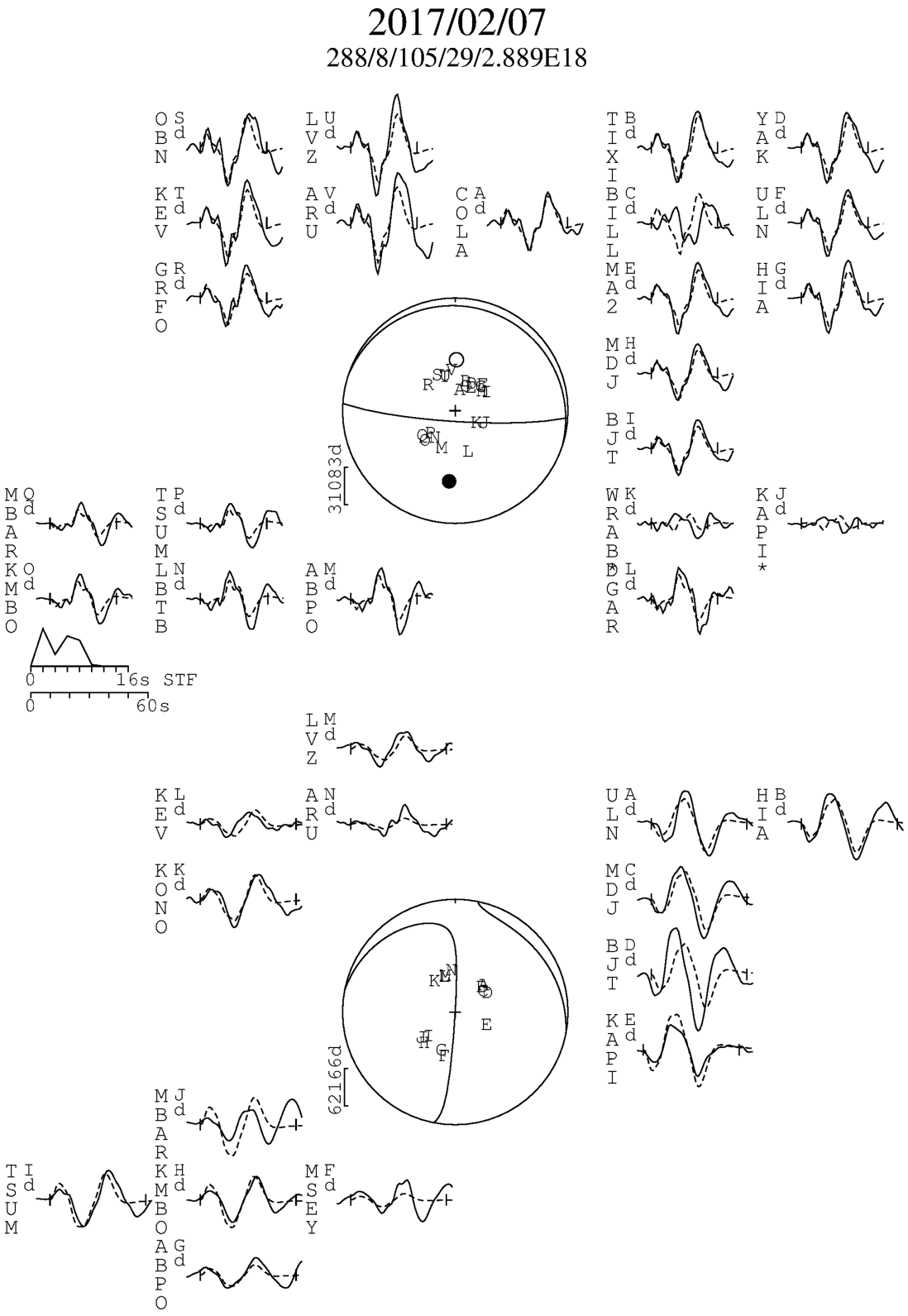

Figure B1. 2017 February 7, offshore central Makran, near Pasni. Numbers under title give source parameters for the minimum misfit solution: strike 288°, dip 8°, rake 105°, depth 29 km and seismic moment 2.89×10^{18} Nm. The source-time function is unusually long for an earthquake of this size, suggesting that this may have been a double event. However, the misfit between the synthetic and observed seismograms is low so any second event is likely to have had a similar focal mechanism. The top panel shows the *P*-wave focal mechanism and *P*-wave arrivals (plotted with twice the magnification of *SH*-wave arrivals), the bottom panel shows the *SH*-wave focal mechanism and *SH*-wave arrivals. Solid lines are recorded seismograms, dashed lines are the synthetics corresponding to the minimum misfit model. The timescale for the seismograms is shown in the bottom right of the top panel, beneath the source-time function. Each station is labelled with a letter which is then plotted on the focal sphere to show the station's location. Stations marked with an asterisk were not included in the inversion. The tension axis is plotted on the focal sphere as an open circle, the pressure axis as a filled circle.

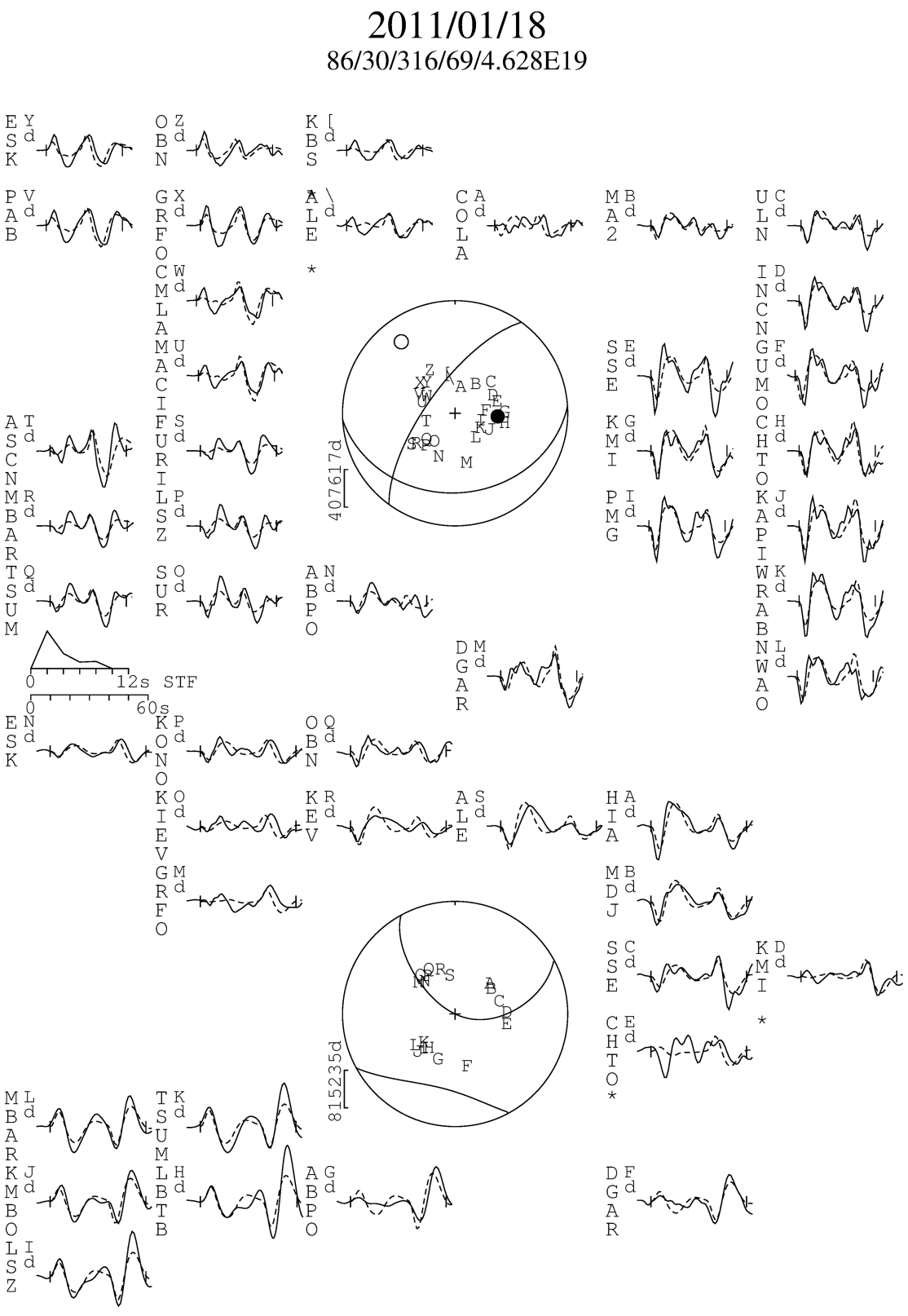

Figure B2. 2011 January 18, northeastern Makran, ~50 km west of Dalbandin. Minimum misfit solution: strike 86°, dip 29°, rake 316°, depth 69 km. Layout as for Fig. B1.

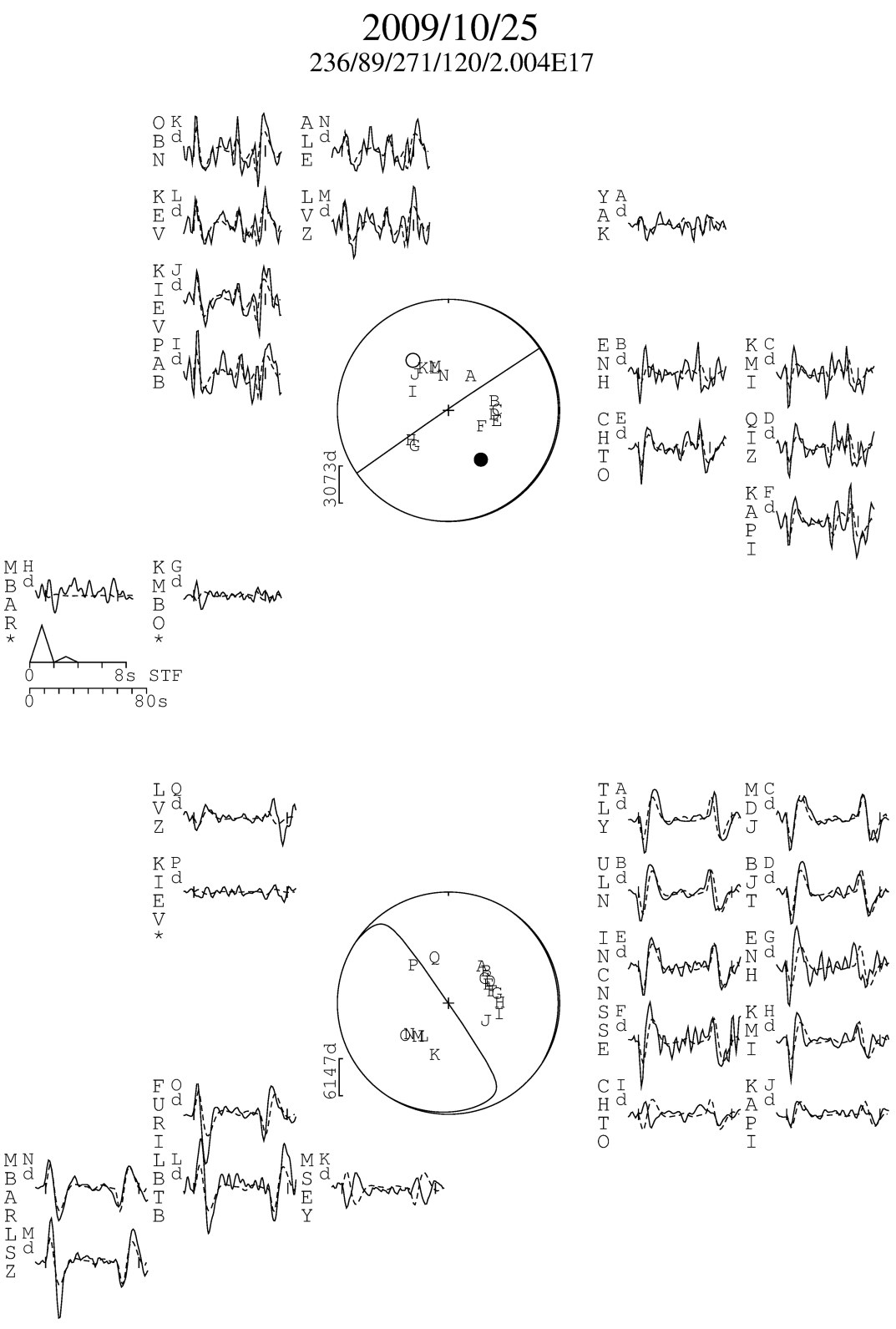

Figure B3. 2009 October 25, southern Afghanistan. Minimum misfit solution: strike 236°, dip 89°, rake 271°, depth 120 km. Layout as for Fig. B1.

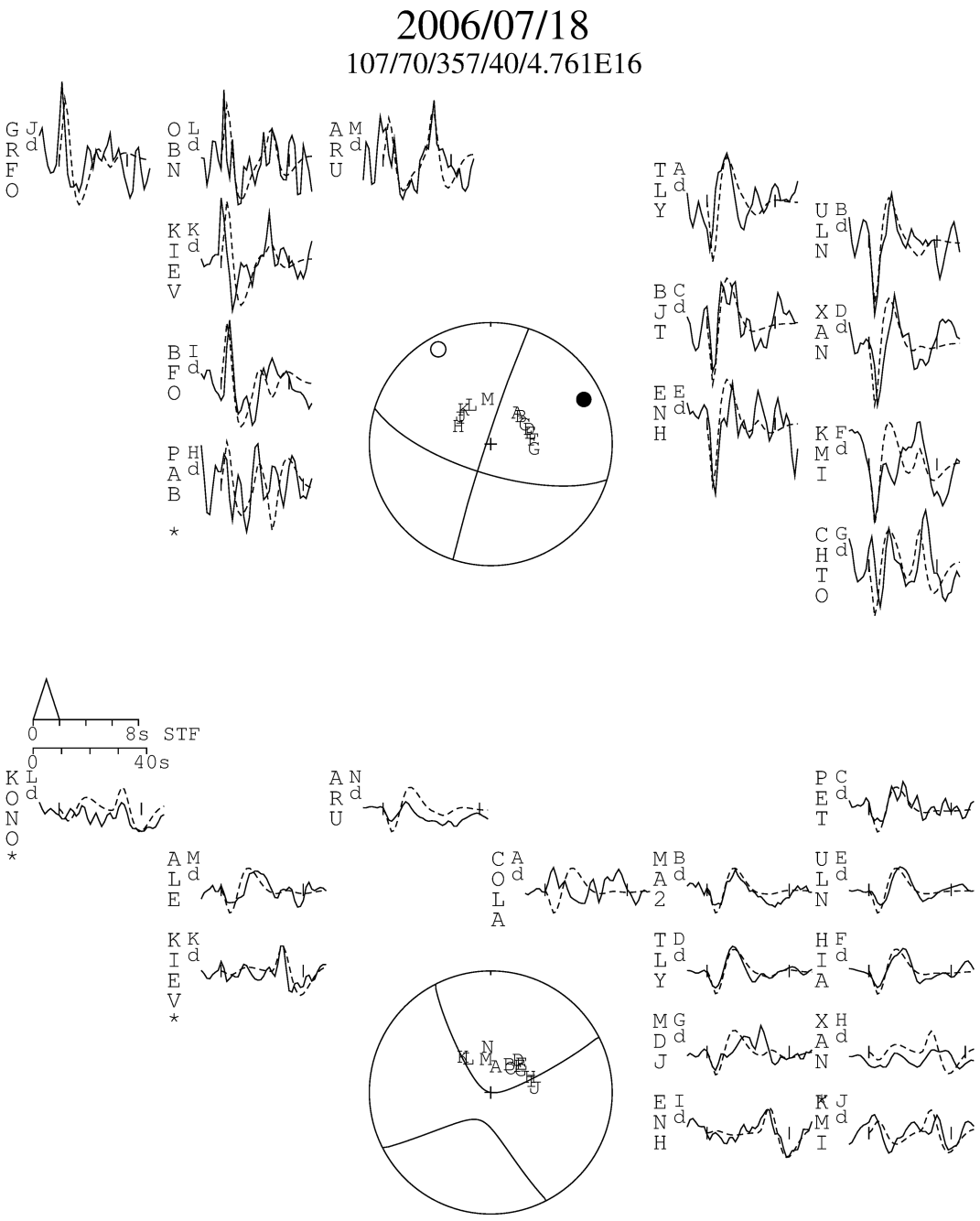

Figure B4. 2006 July 18, central Makran. Minimum misfit solution: strike 107°, dip 70°, rake 357°, depth 40 km. Although many of the waveforms are noisy ARU (*P*), KIEV (*SH*) and ENH (*SH*) provide tight constraints on the depth. Layout as for Fig. B1.

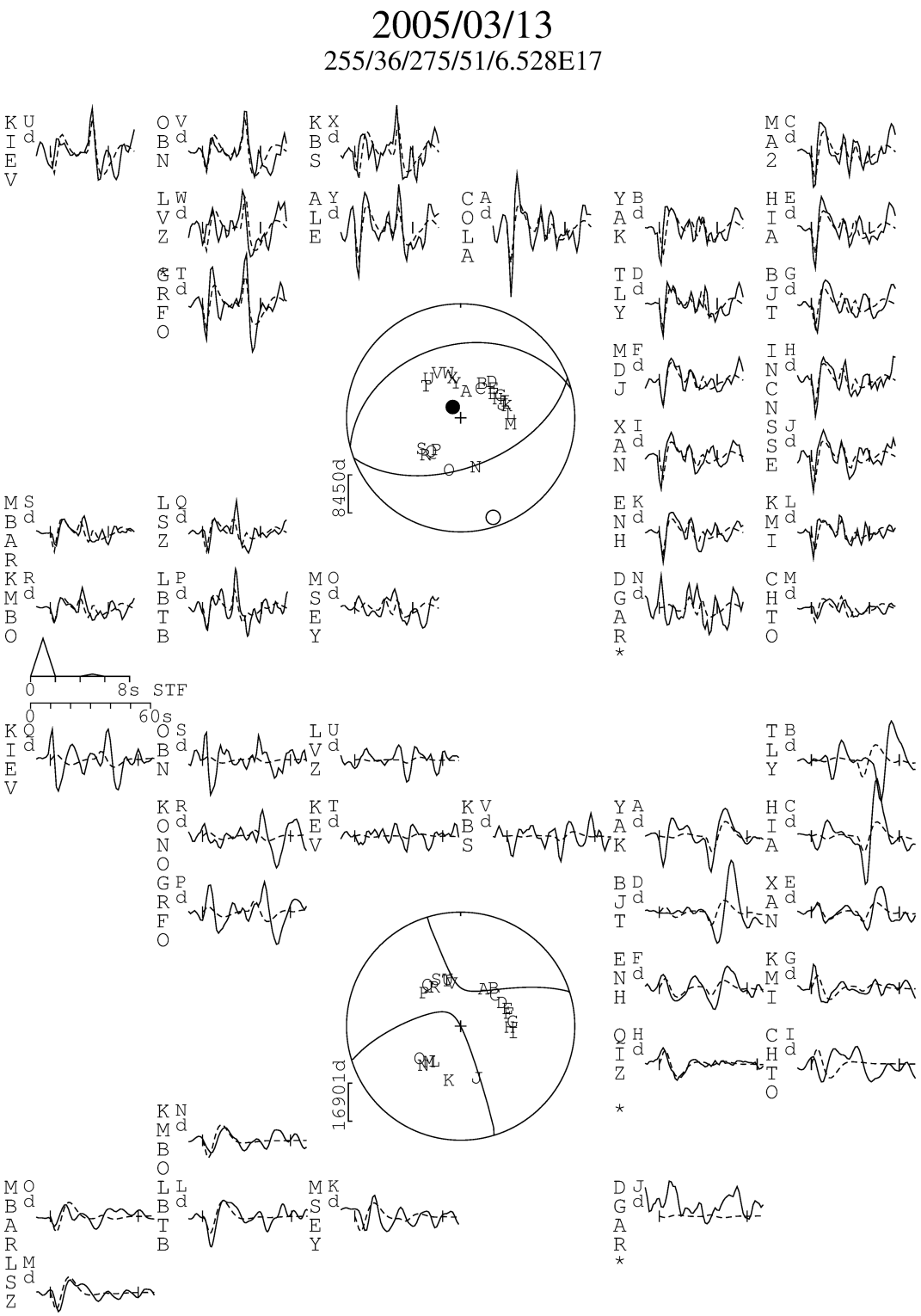

Figure B5. 2005 March 13, north-central Makran, ~50 km W of Saravand. Minimum misfit solution: strike 255°, dip 36°, rake 275°, depth 51 km. Layout as for Fig. B1.

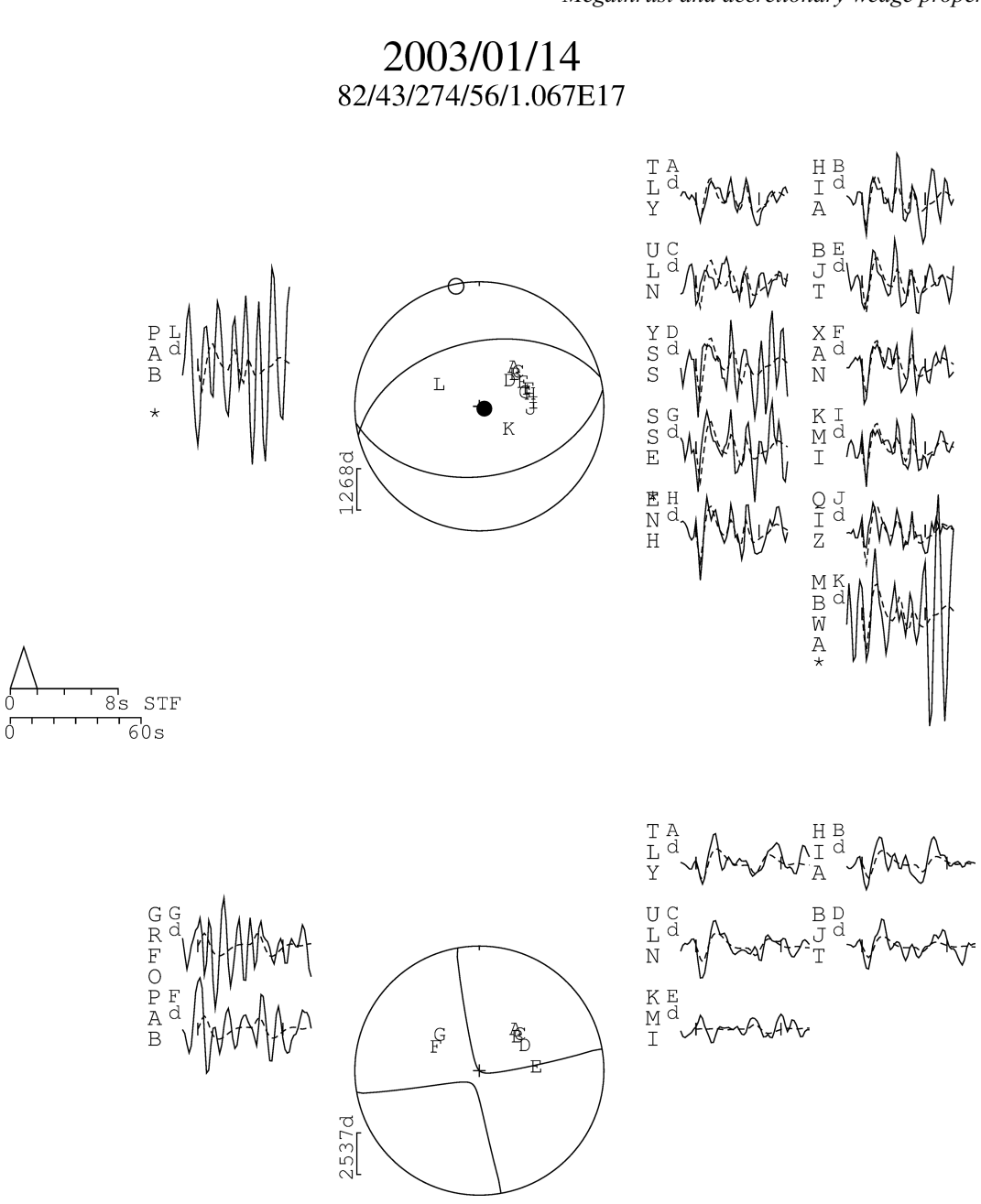

Figure B6. 2003 January 14, north-central Makran, ~100 km E of Khash (the site of a large normal-faulting earthquake in 2013). Minimum misfit solution: strike 82°, dip 43°, rake 274°, depth 56 km. Layout as for Fig. B1.

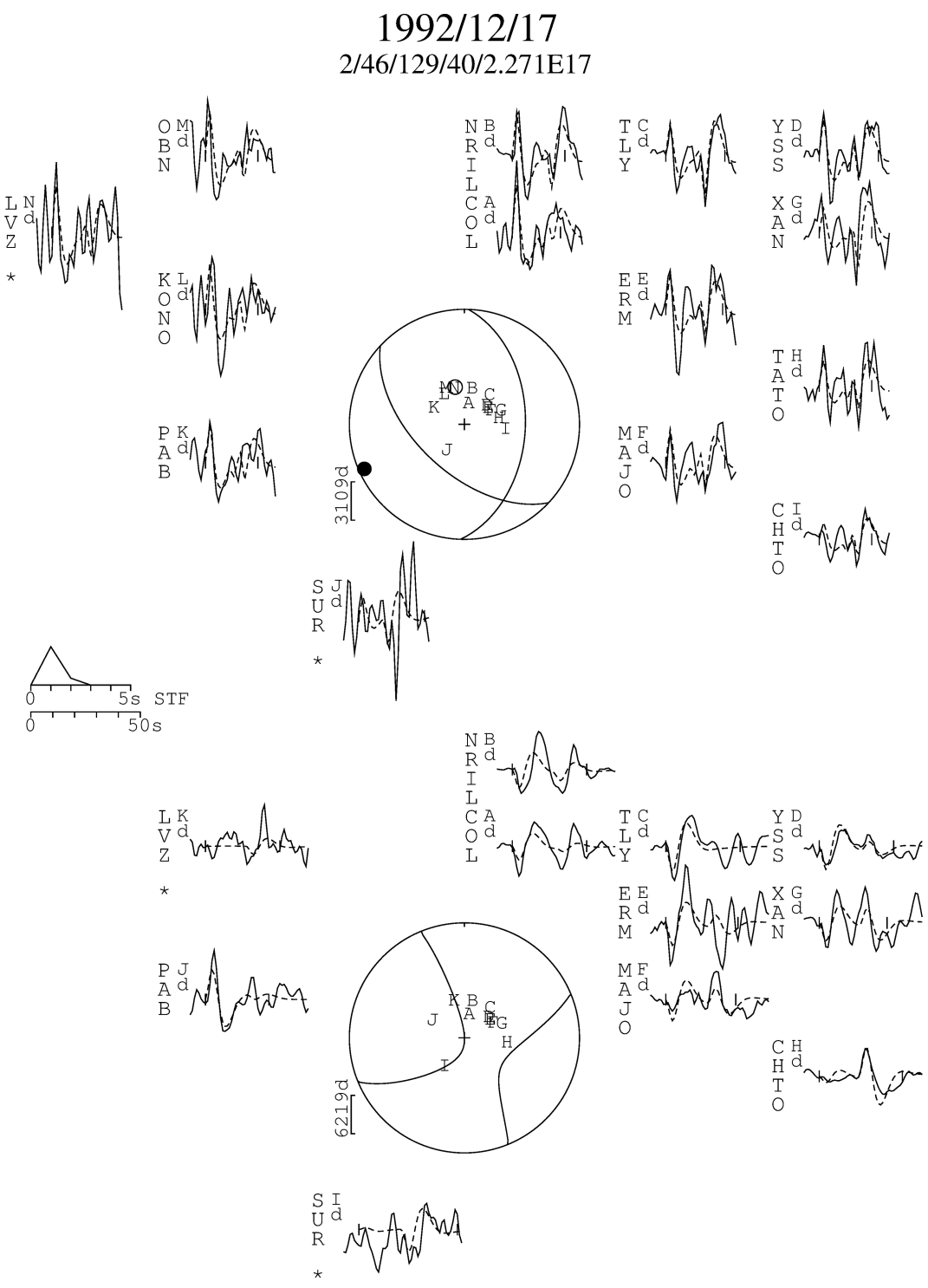

Figure B7. 1992 December 17, central Makran. Minimum misfit solution; strike 2°, dip 46°, rake 40°, depth 40km. Layout as for Fig. B1.

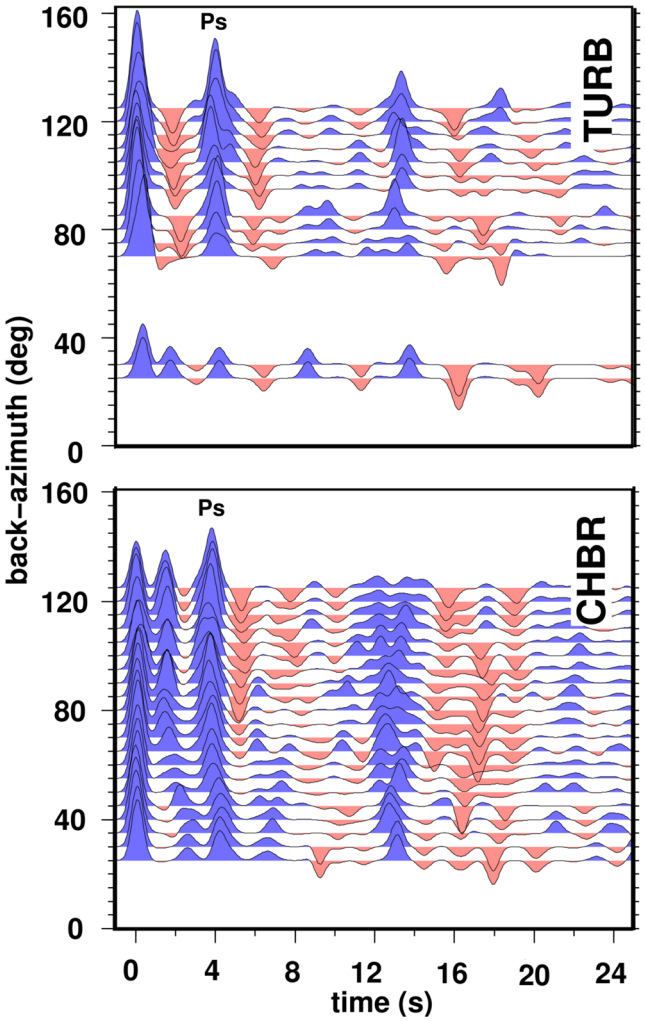

Figure C1. Receiver functions from CHBR and TURB (locations shown in Fig. 1), binned by backazimuth. The strong, positive conversion, labelled Ps, at ∼4 s at both sites is likely to correspond to the top of the subducting Arabian plate.

APPENDIX D: BLOCK ROTATIONS

D1 Vertical-axis rotations

For a series of blocks of length L and width W to accommodate an amount of right-lateral shear, y, they must rotate through an angle θ (Fig. D1), given by

$$\theta = \arcsin\left(\frac{y}{L}\right). \tag{D1}$$

The amount of left-lateral slip on each block-bounding fault, q, is then

$$q = W\tan(\theta). \tag{D2}$$

Although there is no time-dependence in these equations, if y is taken as the per year right-lateral slip then the seismic moment accumulated per year will be

$$M_0 = \mu\, L\, D\, q, \tag{D3}$$

where μ is the shear modulus of the rock, taken here as 3×10^{10}N m^{-2} and D is the downdip width of the fault plane. Substituting eqs (D1) and (D2) into eq. (D3) we find

$$\begin{aligned} M_0 &= \mu\, L\, D\, W\, \tan\left(\arcsin\left(\frac{y}{L}\right)\right) \\ &= \mu\, L\, D\, W\, \tan\left(\arctan\left(\frac{\frac{y}{L}}{\left(\sqrt{1-\left(\frac{y}{L}\right)^2}\right)}\right)\right) \\ &= \frac{\mu\, D\, W\, y}{\sqrt{1-\left(\frac{y}{L}\right)^2}} \\ &= \mu\, D\, W\, y + O\left(\left(\frac{y}{L}\right)^2\right), \end{aligned}$$

that is, to first order the seismic moment is independent of $\frac{y}{L}$, which is small since $L \gg y$.

By considering the number of blocks of given W which can fit between 27°N and the coast, and multiplying the moment accumulated on each fault by the number of blocks, we can estimate the moment accumulated per year across the whole system for a given y. With a distance to the coast λ, the total moment is:

$$\frac{\mu D y \lambda}{\sqrt{1-\left(\frac{y}{L}\right)^2}}$$

which, to first order, is independent of both length and width as discussed in Section 4.2.

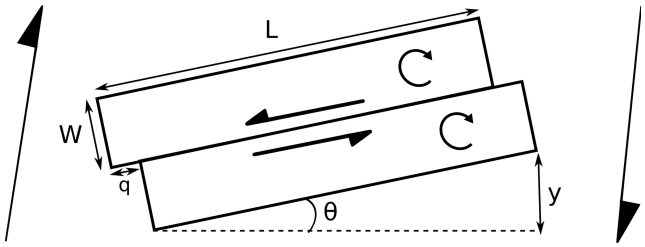

Figure D1. Geometry of vertical-axis rotations accommodating simple shear on horizontal planes. L and W are the block dimensions, q is the amount of slip on the fault between the blocks (if the blocks start aligned), y is the amount of right-lateral shear accommodated and θ is the angle of the blocks anticlockwise from East.

D2 Pure shear block rotations

Fig. D2 shows the detailed geometry of the Hoshab fault's kinematics, described in Section 5.1. Since the 2013 Balochistan earthquake on this fault had a thrust component, we use a reduced value of S, the shortening, such that the total shortening accommodated by thrust faulting and the mechanism shown in this diagram is equal to the GPS shortening rate across the fault (∼10 mm yr^{-1}).

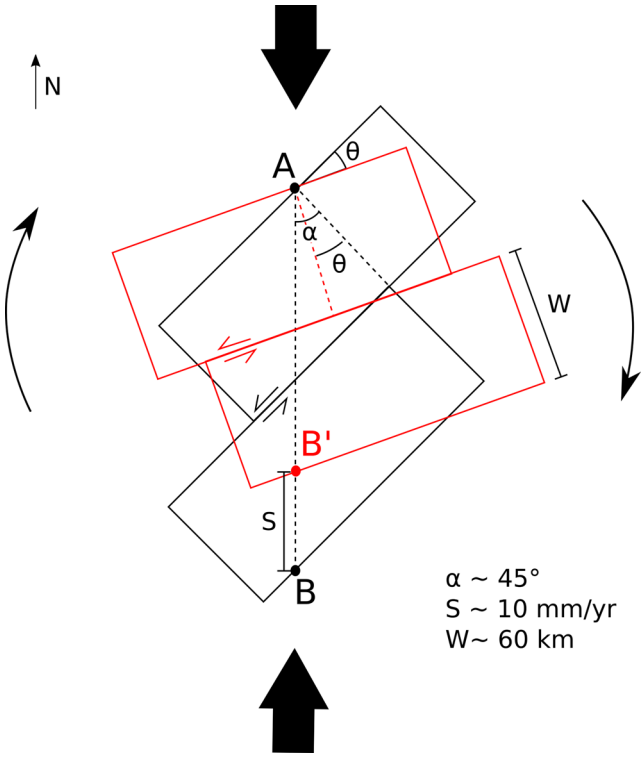

Figure D2. Accommodation of N–S shortening (pure shear) by vertical-axis rotations. Black blocks shows initial configuration, red blocks shows configuration after rotation through an angle θ and slip such that B moves directly towards A. S is the shortening rate across the blocks. For the Hoshab fault, where the 2013 Balochistan earthquake occurred): $W \approx 60$ km, $\alpha \approx 45°$, $S \approx 7$ mm yr^{-1}. This gives a rotation rate of 2.4° Myr^{-1} and a slip rate on the Hoshab fault of ∼10 mm yr^{-1}, if the motion is all on the Hoshab fault. If the motion is distributed across multiple faults each will have a lower slip rate.